

# A Concept for A Dark Matter Detector Using Liquid Helium-4

W. Guo\*

*Mechanical engineering department, Florida State University, Tallahassee, FL 32310, USA*

D.N. McKinsey†

*Physics department, Yale University, New Haven, CT 06520, USA*

(Dated: February 20, 2013)

Direct searches for light dark matter particles (mass  $< 10$  GeV) are especially challenging because of the low energies transferred in elastic scattering to typical heavy nuclear targets. We investigate the possibility of using liquid Helium-4 as a target material, taking advantage of the favorable kinematic matching of the Helium nucleus to light dark matter particles. Monte Carlo simulations are performed to calculate the charge, scintillation, and triplet helium molecule signals produced by recoil He ions, for a variety of energies and electric fields. We show that excellent background rejection can be achieved based on the ratios between different signal channels. We also present some concepts for a liquid-helium-based dark matter detector. Key to the proposed approach is the use of a large electric field to extract electrons from the event site, and the amplification of this charge signal, through proportional scintillation, liquid electroluminescence, or roton emission. The sensitivity of the proposed detector to light dark matter particles is estimated for various electric fields and light collection efficiencies.

PACS numbers: 34.50.Gb, 33.50.-j, 82.20.Pm

## I. INTRODUCTION

Dark matter, while evident on multiple astronomical length scales through its gravitational effects, has an unknown intrinsic nature. Data from primordial nucleosynthesis [1], the cosmic microwave background [2], structure formation [3], and microlensing observations [4] imply that the dark matter cannot be composed of baryons or active neutrinos, implying new physics beyond the Standard Model. Experimental direct detection of dark matter particles, illuminating their mass and interaction properties, would therefore create crucial new scientific understanding in both astrophysics and particle physics.

A particularly compelling model for dark matter is that it consists of Weakly Interacting Massive Particles, or WIMPs [5, 6], with the feature that a massive particle in the early universe interacting through a weak-scale cross-section yields a thermal relic abundance approximately that observed for dark matter. Over the past few decades, models of WIMP dark matter have centered on constrained minimal supersymmetry (CMSSM) models [7], which predict a stable neutralino with mass greater than 40 GeV, limited to higher masses by the requisite mass difference between the chargino and neutralino. Also, it is commonly argued that in the context of supersymmetry it is most natural for the dark matter mass to be comparable to the weak scale [8, 9]. As a result, most direct dark matter experiments have been designed to have excellent sensitivity to dark matter particles with mass comparable to or greater than the

weak scale, yet most of these, including the CDMS [10], ZEPLIN [11], and XENON [12, 13] programs, see no evidence for such high mass dark matter particles, down to the recent XENON100 spin-independent cross-section limit of about  $2 \times 10^{-45}$  cm<sup>2</sup> at 55 GeV [14]. At the same time, the DAMA [15], CoGeNT [16], and CRESST [17] experiments have seen event rate anomalies that can be interpreted in terms of direct detection of light WIMPs, and a number of astrophysical anomalies may be interpreted in terms of light WIMP annihilation[18]. Meanwhile, many new theories of light WIMPs have been developed, and this is currently an area of active development in particle phenomenology. Models for light dark matter often involve a new mediator particle as well as the dark matter itself, and include the next to minimal supersymmetric model (NMSSM) [19], asymmetric dark matter [20], WIMPless dark matter [21], singlet scalars [22], dark sectors with kinetic mixing [23], mirror matter [24]. These models can all evade constraints on light WIMPs from the cosmic microwave background [25], the Large Hadron Collider [26], and Fermi-LAT [27].

Considerable excitement has been generated over the possibility that dark matter particles are relatively low in mass. The difficulty is detecting them, since lighter WIMPs have less kinetic energy and only deposit a small fraction of it when elastically scattering with standard heavy targets like germanium and xenon.

In general it is difficult for heavy targets to be sensitive to light WIMPs, since for typical energy thresholds they are only sensitive to a small part of the WIMP velocity distribution. Models of the WIMP velocity distribution typically assume a Maxwellian distribution of  $f(v) = \exp -(v + v_E)^2/v_0^2$ , where  $v_E \simeq 244$  km/s is the velocity of the Earth around the Milky Way, and  $v_0 \simeq 230$  km/s is the virialized velocity of the average particle that is

\*Electronic address: wguo@magnet.fsu.edu

†Electronic address: daniel.mckinsey@yale.edu

gravitationally bound to the Milky Way [28]. This distribution is expected to be roughly valid up to the Galactic escape velocity  $v_{esc} \simeq 544$  km/s, above which the velocity distribution is zero. A plausible energy threshold for Xe, Ge, and He dark matter experiments is about 5 keVr. But for a 5 GeV WIMP, such as predicted by asymmetric dark matter models [20], its velocity must be particularly large to deposit at least 5 keV. This minimum velocity,  $v_{min}$ , is equal to  $v_{min} = \sqrt{\frac{1}{2} \cdot E_R \cdot M_T / r}$ , where  $E_R$  is the recoil energy,  $r$  is the WIMP-target reduced mass  $r = M_D \cdot M_T / (M_D + M_T)$ ,  $M_D$  and  $M_T$  are the masses of the dark matter particle and the mass of the target nucleus, respectively. For  $E_R$  of 5 keV and  $M_D = 5$  GeV,  $v_{min}$  is equal to 1127, 864, and 427 km/s for Xe, Ge, and He respectively. So for this example,  $v_{min}$  is above  $v_{esc}$  for Xe and Ge, but not for He. The lower limit of the WIMP-target reduced mass that a detector is sensitive to is given by

$$r_{limit} = \frac{1}{v_{esc}} \cdot \sqrt{E_t \cdot M_T / 2}, \quad (1)$$

where  $E_t$  is the energy threshold. So a kinematic figure of merit for light WIMP detection is the product of the energy threshold and the target mass, which should be minimized for the best light WIMP sensitivity.

This challenge of combined low energy threshold and low target mass can likely be met through the use of liquid helium as a target material. In this paper we investigate the use of liquid helium as a target for light dark matter particles in the mass range of 1 to 10 GeV. In Section II we outline the properties of liquid helium in the context of particle detection, in Section III we describe possible configurations of helium-based detectors. The detector can be operated at  $T \sim 3$  K, adopting proportional scintillation or electroluminescence for charge readout; or it can be operated at  $T \sim 100$  mK using bolometers for light and charge readout. In Section IV we examine the sensitivity of liquid helium detectors to light WIMPs. We conclude in Section V.

## II. LIQUID HELIUM AS A DETECTOR MATERIAL

Superfluid helium has been used for a detector material for many applications. Most detector concepts take advantage of the special excitations of the superfluid, and involve detection of phonons, rotons, or quantum turbulence. One example is the HERON concept [29] for pp-solar neutrino detection with rotons in superfluid helium-4 at a temperature of  $\sim 100$  mK. The HERON researchers also considered using such an instrument to look for dark matter [30, 31], with the possibility that the roton/vortex generation by electrons in an applied electric field, combined with prompt roton detection, could be used for particle discrimination. Also, the roton signal could carry information about the nuclear recoil direction. Another is the ULTIMA concept [32] for dark

matter detection with quantized turbulence in superfluid helium-3. Both of these concepts have been the subject of considerable research and development in the past few decades.

Along with its many unusual properties related to superfluidity, liquid helium also produces substantial scintillation light and charge when exposed to ionizing radiation, just like liquid xenon and liquid argon which are already used extensively in the search for dark matter. Some ultracold neutron experiments already make use of the prompt scintillation of liquid helium; for example the measurement of the neutron beta-decay lifetime [33] and search for the neutron permanent electric dipole moment at the Spallation Neutron Source [34, 35]. The prompt scintillation yield in liquid helium is well known, measured by the HERON collaboration to be about 20 photons/keV electron equivalent (keVee).

Depending on particle species, energetic particles elastic scattering in helium can lead to electronic recoils (gamma ray, beta scattering events) or nuclear recoils (neutron or WIMP dark matter scattering events). The recoil electrons or He nucleus collide with helium atoms, producing ionization and excitation of helium atoms along their paths. The ionized electrons can be extracted by an applied electric field. The decay of the helium excimers gives rise to scintillation light. A fraction of the deposited energy is converted into low-energy elementary excitations of the helium, i.e., phonons and rotons. Signals from all these different channels may in principle be used to detect and identify the scattering events. The key for dark matter detection is to be able to suppress the electronic recoils that make up most of the backgrounds from the nuclear recoils that would make up a WIMP signal by use of event discrimination. In this section, we shall estimate the nuclear and electronic recoil signals due to ionization charge, prompt scintillation light, metastable  $\text{He}_2^*$  molecules. We shall present results of Monte Carlo simulations showing that excellent background rejection can be achieved for the purpose of WIMP dark matter detection, based on the ratio between these different signals.

### A. Low energy nuclear recoils in helium

#### 1. Charge exchange processes

A WIMP dark matter scattering event in liquid helium would result a recoil helium nuclei. Depending on the energy involved in the scattering process, the recoil He can be a bare ion ( $\text{He}^{2+}$ ) or a dressed ion ( $\text{He}^{1+}$ ), or even a neutral helium atom ( $\text{He}^0$ ). The recoil He dissipates its kinetic energy through collisions with ground state He atoms. Such collisions can be elastic or inelastic that lead to ionization or excitation of He atoms. The ionization and excitation cross-sections are different for the recoil He ion in different charge states. As the fast recoil He ion slows down, interactions involving electron

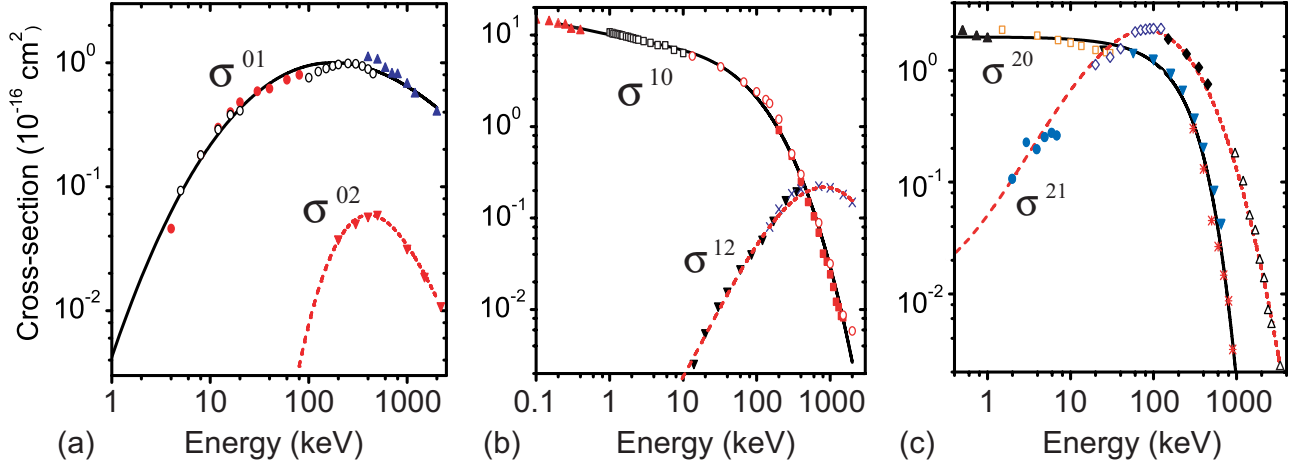


FIG. 1: (color online). Charge exchange cross sections due to  $\text{He}^0$ ,  $\text{He}^{1+}$ , and  $\text{He}^{2+}$  interacting with ground state He atoms. The curves were fitted to experimental data by polynomial functions. (a)  $\sigma^{01}$ : — (this work),  $\bullet$  (Ref. [36]),  $\circ$  (Ref. [37]),  $\blacktriangle$  (Ref. [38]);  $\sigma^{02}$ : - - - (this work),  $\blacktriangledown$  (Ref. [38]). (b)  $\sigma^{10}$ : — (this work),  $\blacktriangle$  (Ref. [39]),  $\square$  (Ref. [40]),  $\circ$  (Ref. [41]),  $\blacksquare$  (Ref. [42]);  $\sigma^{12}$ : - - - (this work),  $\blacktriangledown$  (Ref. [43]),  $\times$  (Ref. [41]). (c)  $\sigma^{20}$ : — (this work),  $\blacktriangle$  (Ref. [44]),  $\square$  (Ref. [45]),  $\blacktriangledown$  (Ref. [46]),  $*$  (Ref. [47]);  $\sigma^{21}$ : - - - (this work),  $\bullet$  (Ref. [48]),  $\diamond$  (Ref. [49]),  $\blacklozenge$  (Ref. [50]),  $\triangle$  (Ref. [51]).

capture and loss by the projectile become an increasingly important component of the energy loss process. Charge transfer can produce residual ions without the release of free electrons, and free electrons can be ejected from the moving ion (or neutral) with no residual ions being formed.

Charge transfer cross sections are generally designated as  $\sigma^{if}$  where  $i$  represents the initial charge state of the moving ion, and  $f$  is the charge state after the collision. For a complete description of the full slowing down of a recoil He, we need cross sections for one-electron capture  $\sigma^{21}$  and two-electron capture  $\sigma^{20}$  for  $\text{He}^{2+}$ , one-electron capture  $\sigma^{10}$  and one-electron loss  $\sigma^{12}$  for  $\text{He}^{1+}$ , and one-electron loss  $\sigma^{01}$  and two-electron loss  $\sigma^{02}$  for  $\text{He}^0$ . In Fig. 1, we show the six charge exchange cross-sections based on available experimental data for  $\text{He}^0$ ,  $\text{He}^{1+}$  and  $\text{He}^{2+}$ . These cross sections were least-squares fitted by simple polynomial functions of the form  $\log(\sigma^{if}) = \sum_n C_n (\log E)^n$ , where the  $C_n$ 's are the fitting parameters, and  $E$  is the particle energy in keV. Smooth extrapolation was carried out where the experimental data were lacking. Following the method by Allison [50], the fractions  $F_0$ ,  $F_1$ , and  $F_2$  that the moving particle to be found in charge state 0, 1, and 2 are given by

$$\begin{aligned} dF_0/dz &= N[-F_0(\sigma^{01} + \sigma^{02}) + F_1\sigma^{10} + F_2\sigma^{20}] \\ dF_1/dz &= N[-F_1(\sigma^{10} + \sigma^{12}) + F_0\sigma^{01} + F_2\sigma^{21}] \\ F_2 &= 1 - F_0 - F_1 \end{aligned} \quad (2)$$

where  $N \simeq 2.2 \times 10^{22} \text{ cm}^{-3}$  is the number density of liquid helium and  $z$  is the path length along the particle track. If the charge exchange cross-sections  $\sigma^{if}$  do not vary as the He ion moves, the equilibrium charge fractions  $F_0^\infty$ ,  $F_1^\infty$ , and  $F_2^\infty$  as  $z \rightarrow \infty$  are given by Allison [50]

as follows:

$$\begin{aligned} F_0^\infty &= (f\sigma^{21} - a\sigma^{20})/D \\ F_1^\infty &= (b\sigma^{20} - g\sigma^{21})/D \\ F_2^\infty &= [(a-b)\sigma^{20} + g(a+\sigma^{21}) - f(b+\sigma^{21})]/D \end{aligned} \quad (3)$$

in which

$$\begin{aligned} a &= -(\sigma^{10} + \sigma^{12} + \sigma^{21}), \quad b = \sigma^{01} - \sigma^{21}, \\ f &= \sigma^{10} - \sigma^{20}, \quad g = -(\sigma^{01} + \sigma^{02} + \sigma^{20}), \\ D &= ag - bf \end{aligned} \quad (4)$$

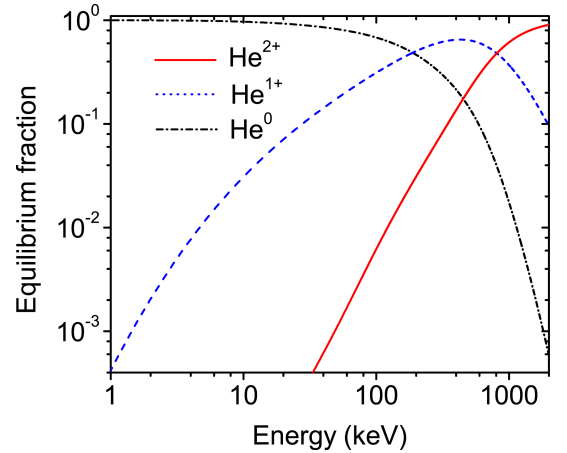


FIG. 2: (color online) Equilibrium fractions of the charge states of an energetic helium ion in liquid helium.

Fig. 2 shows the calculated equilibrium charge fractions as a function of helium ion energy based on Eq. 3 and Eq. 4. At energy higher than a few thousands of keV, the helium ion appears primarily as a bare ion  $\text{He}^{2+}$ ,

whereas in low energy regime ( $< 100$  keV) the fraction of charge zero state  $\text{He}^0$  dominates. These results are derived based on the assumption that  $\sigma^{if}$  does not vary as the He ion moves. In reality, since the charge exchange cross-sections depend on particle energy, as a He ion slows down in liquid helium, the  $\sigma^{if}$  in Eq. 2 should change as  $z$  varies. In this situation, a full description of variation of the charge fractions  $F_0$ ,  $F_1$ , and  $F_2$  is given by the following equations

$$\begin{aligned} \frac{dF_0(E)}{dE} &= \frac{N}{S(E)} [-F_0(\sigma^{01} + \sigma^{02}) + F_1\sigma^{10} + F_2\sigma^{20}] \\ \frac{dF_1(E)}{dE} &= \frac{N}{S(E)} [-F_1(\sigma^{10} + \sigma^{12}) + F_0\sigma^{01} + F_2\sigma^{21}] \\ F_2(E) &= 1 - F_0(E) - F_1(E) \end{aligned} \quad (5)$$

where  $S(E)=dE/dz$  is the total stopping power of a He ion in liquid helium that describes the average energy loss of the He ion per unit path length.  $S(E)$  is the sum of the electronic stopping power  $S_e(E)$  (energy loss due to the inelastic collisions between bound electrons in the medium and the ion) and the nuclear stopping power  $S_n(E)$  (energy loss due to the elastic collisions between the helium atoms and the ion). Fig. 3 shows the stop-

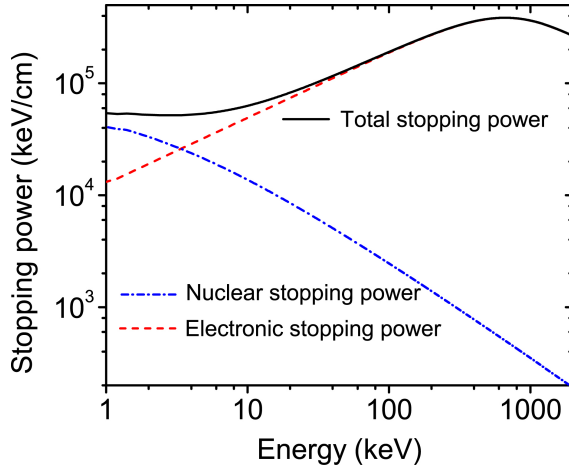


FIG. 3: (color online) Stopping power of a He ion in liquid helium. Data are drawn from the National Institute of Standards and Technology (NIST) database [52].

ping power data drawn from the National Institute of Standards and Technology (NIST) database [52]. Knowing the stopping power  $S(E)$  and the charge exchange cross-sections  $\sigma^{if}(E)$ , one can integrate Eq. 5 to calculate the energy dependence of the fractions of different charge states with a given initial condition. An example is shown in Fig. 4. We see that if we start with a bare ion  $\text{He}^{2+}$  ( $F_2 = 1$ ) at an initial kinetic energy of 50 keV, as the ion slows down the fractions of the different charge states  $F_0$ ,  $F_1$ , and  $F_2$  quickly evolve to the equilibrium values. This is because that due to the relatively large charge exchange cross-sections and the high helium number density, many charge exchange collisions can take place in a short path-length of the fast He ion.

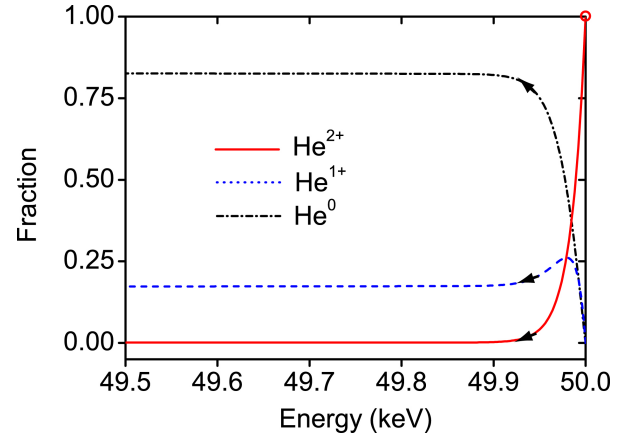


FIG. 4: (color online) Fractions of the charge states of an energetic helium ion as it slows down in liquid helium. The ion started as a  $\text{He}^{2+}$  with initial energy of 50 keV, as indicated by the red circle. The arrows show how the fractions evolve as the particle loses its energy.

To achieve the equilibrium charge fractions, only a few charge exchange collisions are needed and the energy loss in this process is small. As a consequence, we can safely use the equilibrium fractions of the charge states to study the slowing down of a fast He ion in liquid helium, with no need to consider the initial charge states.

## 2. Ionization and excitation yields

The ionization and excitation yields due to a recoil helium nuclei moving in liquid helium are important premise parameters needed for the design of a helium-based dark matter detector. Sato *et al.* [53] have studied the ionization and excitation yields of an alpha particle ( $\text{He}^{2+}$ ) in liquid helium using the collision cross sections derived with the binary encounter theory [54]. In their analysis, the charge exchange collisions are ignored and the fraction of the alpha particle energy that is lost to elastic collisions with surrounding He atoms (nuclear stopping) is not included. Nuclear stopping can become dominant when the alpha particle energy is small, which is known as the Lindhard effect [55]. The energy of a recoil helium nuclei in a WIMP scattering event is expected to be relatively low ( $\lesssim 100$  keV). To obtain more reliable estimation of the ionization and excitation yields from a recoil helium nuclei, we present an analysis that systematically accounts for both the charge exchange processes and the Lindhard effect.

Assuming a continuous slowing down, the total number of free electrons  $N_{e1}$  produced along the path of a recoil

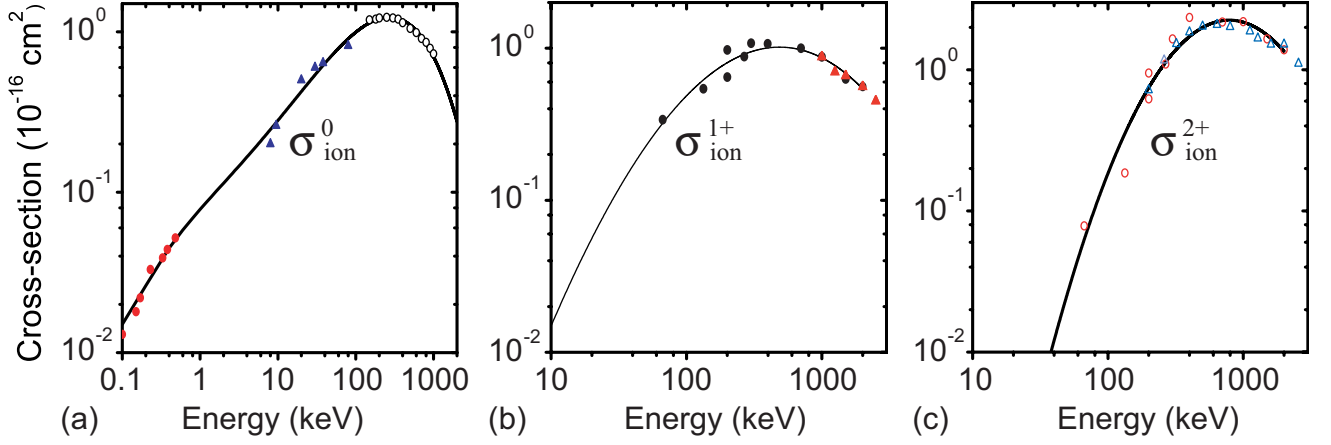


FIG. 5: (color online). Ionization cross-sections due to  $\text{He}^0$ ,  $\text{He}^{1+}$ , and  $\text{He}^{2+}$  interacting with ground state He atoms. The curves were fitted to experimental data by polynomial functions. (a)  $\sigma_{\text{ion}}^0$ : — (this work),  $\bullet$  (Ref. [56]),  $\blacktriangle$  (Ref. [57]),  $\circ$  (Ref. [58]). (b)  $\sigma_{\text{ion}}^{1+}$ : — (this work),  $\bullet$  (Ref. [59]),  $\blacktriangle$  (Ref. [60]). (c)  $\sigma_{\text{ion}}^{2+}$ : — (this work),  $\circ$  (Ref. [59]),  $\blacktriangle$  (Ref. [61]).

He nuclei with an initial kinetic energy  $E$  is given by

$$\begin{aligned}
 N_{\text{el}} &= N_{\text{el}}^{\text{Dir}} + N_{\text{el}}^{\text{Exc}} + N_{\text{el}}^{\text{Sec}} \\
 &= \int_0^E \frac{NdE'}{S(E')} [F_0^\infty(E')\sigma_{\text{ion}}^0 + F_{1+}^\infty(E')\sigma_{\text{ion}}^{1+} + F_{2+}^\infty(E')\sigma_{\text{ion}}^{2+}] \\
 &\quad + \int_0^E \frac{NdE'}{S(E')} [F_0^\infty(E')(\sigma^{01} + 2\sigma^{02}) + F_{1+}^\infty(E')\sigma^{12}] \\
 &\quad + N_{\text{el}}^{\text{Sec}}
 \end{aligned} \tag{6}$$

Here  $N_{\text{el}}^{\text{Dir}}$  and  $N_{\text{el}}^{\text{Exc}}$  are the number of electrons produced in direct ionization and in charge exchange processes due to He ion impact, and are given by the first and the second integral terms on the right side of the equation.  $\sigma_{\text{ion}}^0$ ,  $\sigma_{\text{ion}}^{1+}$ , and  $\sigma_{\text{ion}}^{2+}$  are the direct ionization cross sections due to  $\text{He}^0$ ,  $\text{He}^{1+}$ , and  $\text{He}^{2+}$  interacting with ground state He atoms, respectively.  $N_{\text{el}}^{\text{Sec}}$  is the number of ionizations produced by secondary electrons that have energy higher than the ionization threshold of a He atom (24.6 eV).  $F_i^\infty$  ( $i = 0, 1, 2$ ) is the equilibrium fraction of charge state  $i$  as given by Eq. 3. The ratio of  $N_{\text{el}}^{\text{Sec}}$  to  $N_{\text{el}}$  decreases with decreasing  $E$  and is only a few percent when  $E \sim 100$  keV [53]. We shall neglect  $N_{\text{el}}^{\text{Sec}}$  in the following analysis for simplicity. To estimate the ionization yield, defined as  $Y_{\text{el}} = N_{\text{el}}/E$ , the values of the direct ionization cross sections are needed. In Fig. 5 the experimental data for  $\sigma_{\text{ion}}^0$ ,  $\sigma_{\text{ion}}^{1+}$ , and  $\sigma_{\text{ion}}^{2+}$  are shown. We again fit the experimental data by simple polynomial functions  $\log(\sigma_{\text{ion}}) = \sum_n C'_n (\log E)^n$ , and extrapolate the curves where the experimental data were lacking. From Fig. 2 one can see that at  $E \lesssim 100$  keV, the fraction of the charge zero state ( $\text{He}^0$ ) dominates. The available ionization and charge exchange cross section data for  $\text{He}^0$  in the energy range of 0.1~100 keV allow us to make reliable fit and extrapolation for analyzing the ionization yield. The calculated ionization yield  $Y_{\text{el}}$  of a recoil He ion as a function of the ion energy is shown in Fig. 6 as the black solid curve.

The total number of excitations  $N_{\text{ex}}$  produced by a

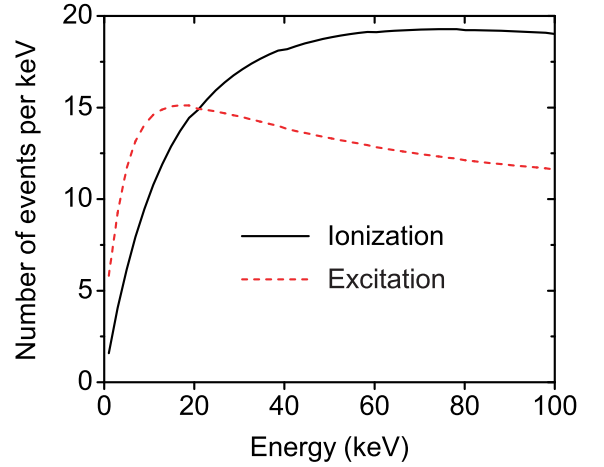


FIG. 6: (color online) Ionization and excitation yields of a recoil He ion in liquid helium as a function of the He ion energy.

recoil He nuclei with an initial kinetic energy  $E$  is given by

$$\begin{aligned}
 N_{\text{ex}} &= \int_0^E \frac{NdE'}{S(E')} [F_0^\infty(E')\sigma_{\text{ex}}^0 + F_{1+}^\infty(E')\sigma_{\text{ex}}^{1+} \\
 &\quad + F_{2+}^\infty(E')\sigma_{\text{ex}}^{2+}] + \tilde{N}_{\text{ex}}
 \end{aligned} \tag{7}$$

where  $\sigma_{\text{ex}}^0$ ,  $\sigma_{\text{ex}}^{1+}$ , and  $\sigma_{\text{ex}}^{2+}$  are the total excitation cross sections due to  $\text{He}^0$ ,  $\text{He}^{1+}$ , and  $\text{He}^{2+}$  interacting with ground state He atoms, respectively. Here  $\tilde{N}_{\text{ex}}$  is the number of excitations produced by secondary electrons, which can again be neglected at  $E \lesssim 100$  keV [53]. Experimental excitation cross section data are limited. For instance, Kempter *et al.* estimated the excitation cross sections due He atom impact, but only with collision energy below 600 eV [62]; De Heer and Van Den Bos measured the excitation cross sections for  $\text{He}^{1+}$  incident on He, but only for excitations to states with principle



quantum number  $n \geq 3$  [63]. Instead of fitting the data to obtain the excitation cross sections, we estimate the excitation yield  $Y_{\text{ex}} = N_{\text{ex}}/E$  based on the known electronic stopping power as follows. The electronic stopping power  $S_e(E)$  can be written as

$$\begin{aligned} \frac{S_e}{N} = & F_0^\infty [\sigma_{\text{ion}}^0 (Q_{\text{He}} + \bar{\varepsilon}_0) + \sigma_{\text{ex}}^0 \bar{Q}_{\text{ex}} + (\sigma^{01} + 2\sigma^{02})(Q_{\text{He}} + \lambda E)] \\ & + F_1^\infty [\sigma_{\text{ion}}^{1+} (Q_{\text{He}} + \bar{\varepsilon}_1) + \sigma_{\text{ex}}^{1+} \bar{Q}_{\text{ex}} + \sigma^{12}(Q_{\text{He}} + \lambda E)] \\ & + F_2^\infty [\sigma_{\text{ion}}^{2+} (Q_{\text{He}} + \bar{\varepsilon}_2) + \sigma_{\text{ex}}^{2+} \bar{Q}_{\text{ex}}] \end{aligned} \quad (8)$$

Here  $Q_{\text{He}} = 24.6$  eV is the ionization energy of a helium atom.  $\bar{\varepsilon}$  is the average kinetic energy of secondary electrons by He ion impact.  $\bar{Q}_{\text{ex}} = \sum Q_{ij} \sigma_{ij} / \sum \sigma_{ij}$  is the mean excitation energy where  $Q_{ij}$  and  $\sigma_{ij}$  are the He( $i \rightarrow j$ ) excitation energy and the associated cross section, respectively. Lack of detailed information, here we assume  $\bar{Q}_{\text{ex}}$  to be the same for the incident He ion in different charge states.  $\lambda = m_e/m_{\text{He}} \simeq 1.36 \times 10^{-4}$  where  $m_e$  and  $m_{\text{He}}$  are the masses of an electron and a He atom, respectively. In Eq. 8, the energy transfer model is assumed such that in a charge-loss collision, a stripped electron is ejected from the projectile with nearly the same velocity as the projectile. Indeed the stripped electrons are observed in the spectrum of secondary electrons produced when He ion impacts on water vapor as a peak centered at  $\lambda E$  [64]. An energy deposition of  $Q_{\text{He}} + \lambda E$  is thus made when an electron is lost from the projectile [65]. In an electron capture process, energy deposition is essentially due to the recoil of the ionized He atom and is negligible. As a result, the terms in the square brackets in Eq. 7 can be derived based on Eq. 8

$$\begin{aligned} & F_0^\infty \sigma_{\text{ex}}^0 + F_1^\infty \sigma_{\text{ex}}^{1+} + F_2^\infty \sigma_{\text{ex}}^{2+} \\ = & \frac{1}{Q_{\text{ex}}} \left\{ \frac{S_e}{N} - F_0^\infty [\sigma_{\text{ion}}^0 (Q_{\text{He}} + \bar{\varepsilon}_0) + (\sigma^{01} + 2\sigma^{02})(Q_{\text{He}} + \lambda E)] \right. \\ & - F_1^\infty [\sigma_{\text{ion}}^{1+} (Q_{\text{He}} + \bar{\varepsilon}_1) + \sigma^{12}(Q_{\text{He}} + \lambda E)] \\ & \left. - F_2^\infty [\sigma_{\text{ion}}^{2+} (Q_{\text{He}} + \bar{\varepsilon}_2)] \right\} \end{aligned} \quad (9)$$

Plugging Eq. 9 back into Eq. 7, the excitation yield can be derived as

$$\begin{aligned} Y_{\text{ex}} \simeq & \frac{L}{Q_{\text{ex}}} - \frac{Q_{\text{He}}}{Q_{\text{ex}}} Y_{\text{el}} - \frac{1}{E} \int_0^E \frac{N dE'}{S(E')} \frac{1}{Q_{\text{ex}}} \cdot \\ & \{ [F_0^\infty \sigma_{\text{ion}}^0 \bar{\varepsilon}_0 + F_1^\infty \sigma_{\text{ion}}^{1+} \bar{\varepsilon}_1 + F_2^\infty \sigma_{\text{ion}}^{2+} \bar{\varepsilon}_2] \\ & + [F_0^\infty (\sigma^{01} + 2\sigma^{02}) \lambda E + F_1^\infty \sigma^{12} \lambda E] \} \end{aligned} \quad (10)$$

in which  $L$  is the Lindhard factor, defined as

$$L = \frac{1}{E} \int_0^E \frac{S_e(E') dE'}{S(E')}. \quad (11)$$

Lindhard factor designates the ratio of the energy given to the electronic collisions to the total energy. A plot of the Lindhard factor as a function of the recoil He ion energy is shown in Fig. 7. Since only the part of energy given to the electronic collisions can be used as ionization and scintillation signals, the Lindhard factor  $L$  is important for the determination of the sensitivity of WIMP detectors.

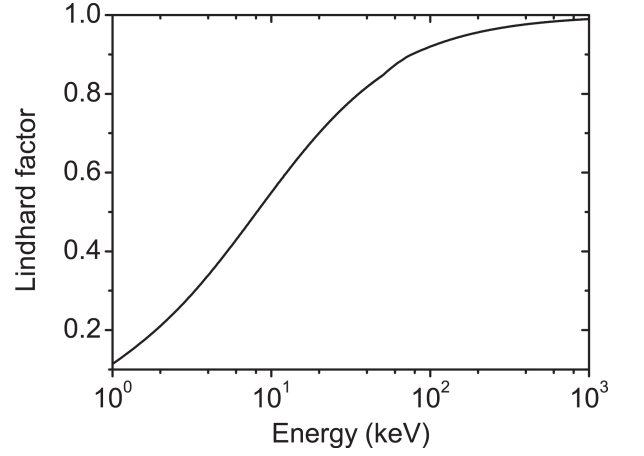


FIG. 7: Calculated Lindhard factor for a recoil He ion in liquid helium as a function of the He ion energy.

In order to calculate  $Y_{\text{ex}}$  using Eq. 10, we need to make further approximations on  $\bar{Q}_{\text{ex}}$  and  $\bar{\varepsilon}$ . Since the dominant excitation process in low energy collisions between He atoms and the projectile is He( $1s^2 \rightarrow 1s2p$ ) with an excitation energy of 21.2 eV [62], we take  $\bar{Q}_{\text{ex}} \simeq 21$  eV for simplicity. The average energy  $\bar{\varepsilon}$  of the secondary electrons can be expanded in power series of  $E$ . To the lowest order in  $E$ , we may write  $\bar{\varepsilon} \simeq \gamma(E - 24.6 \text{ eV})$  for  $E > 24.6$  eV. Linear dependence of  $\bar{\varepsilon}$  on  $E$  is evidenced for secondary electrons ejected by helium ion impact on water vapor with energy  $E \lesssim 100$  keV [65]. Furthermore, at small  $E$ ,  $\bar{\varepsilon}$  is similar for He ion impact in different charge states. We choose  $\gamma = 0.3$  for all charge states such that the ratio between the calculated ionization yield  $Y_{\text{el}}$  and excitation yield  $Y_{\text{ex}}$  agrees with Sato *et al*'s result at  $E \sim 100$  keV where the Lindhard effect is mild. Note that variation of  $\gamma$  does not affect  $Y_{\text{ex}}$  at small  $E$ . The calculated  $Y_{\text{ex}}$  is shown in Fig. 6 as the red dashed curve.

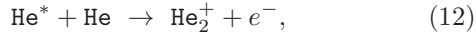
The drop of both the ionization yield and the excitation yield at energies lower than about 50 keV is due to the drop of the electronic collision cross sections in this energy regime, as well as the loss of the He ion energy to elastic nuclear collisions (Lindhard effect). As a comparison, for an energetic electron moving in LHe, Sato *et al* [53, 66] estimated that the total ionization yield and excitation yield are nearly constant ( $Y_{\text{el}}^{(e)} \simeq 22.7 \text{ keV}^{-1}$  and  $Y_{\text{ex}}^{(e)} \simeq 10.2 \text{ keV}^{-1}$ ) in the energy range from a few hundred keV down to about 1 keV.

## B. Signals in liquid helium

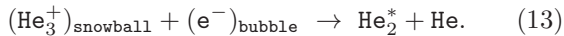
### 1. Charge signal

Electrons and helium ions are produced along the track of an energetic particle as a consequence of ionization or charge-exchange collisions. Beside these processes, ex-

cited helium atoms produced by the projectile with principal quantum number  $n \geq 3$  can autoionize in liquid helium by the Hornbeck-Molnar process [67]



since the 2 eV binding energy of  $\text{He}_2^+$  is greater than the energy to ionize a  $\text{He}(n \geq 3)$  atom. Based on the oscillator strengths for the transitions between the ground state and the various excited states of helium [68], slightly more than one third of the atoms promoted to excited states will have a principal quantum number of 3 or greater. All these electrons and ions quickly thermalize with the liquid helium. The ions form helium “snowballs” in a few picoseconds [69], and they do not move appreciably from the sites where they are originated. On the other hand, as the energy of the free electrons drops below about 20 eV, the only process by which they can lose energy is elastic scattering from helium atoms. Due to the low energy-transfer efficiency (about  $\lambda = 1.36 \times 10^{-4}$  per collision), these electrons make many collisions and undergo a random walk till their energy drops below 0.1 eV, the energy thought to be necessary for bubble state formation. Once thermalized, the electrons form bubbles in the liquid typically within 4 ps [70]. Due to the Coulomb attraction, electron bubbles and helium ion snowballs recombine in a very short time and lead to the production of  $\text{He}_2^*$  excimer molecules



When an external electric field is applied, some of the electrons can escape the recombination and be extracted.

At temperatures above 1 K, electron bubbles essentially move along the electric field lines in the moving frame of the ions due to the viscous damping [71, 72]. In this situation, the fraction  $q$  of the electrons that can be extracted under an applied field  $\varepsilon$  depends largely on the initial electron-ion separation and the ionization density along the projectile track. The mean electron-ion separation has been determined to be about 60 nm for both beta particle ionization events [72] and alpha particle ionization events [73]. The energy deposition rate for an electron of several hundred keV is approximately 50 eV/micron, whereas for an alpha particle of a few MeV the rate is 25 keV/micron [74]. The average energy needed to produce an electron-ion pair has been measured to be about 42.3 eV for a beta particle [75] and about 43.3 eV [76] for an alpha particle. It follows that charge pairs are separated on average about 850 nm along a beta particle track and only about 1.7 nm along the track of an energetic alpha particle. The recombination along a beta particle track where the electron-ion pairs are spatially separated is described by Onsager’s geminate recombination theory [77]. For the highly ionizing track of an alpha particle in liquid helium, the electrons feel the attraction from all nearby ions and are harder to be extracted. Jaffe’s columnar theory of recombination is more applicable in this situation [78, 79]. In Fig. 8,

the charge extraction from a beta particle track, simulated by Guo *et al.* [72], and that from an alpha particle track, simulated by Ito *et al.* [73], are shown as the blue solid curve and the red dashed curve, respectively. Note that in the low field regime, the measured charge collection by Ghosh [80] and Sethumadhavan [81] for beta particles is higher than the predicted result by Guo *et al.* [72]. Furthermore, these charge extraction analyses are for temperatures above 1 K. At very low temperatures, the ionized electrons can stray away from the field lines which enhances the charge extraction at a given applied field [72].

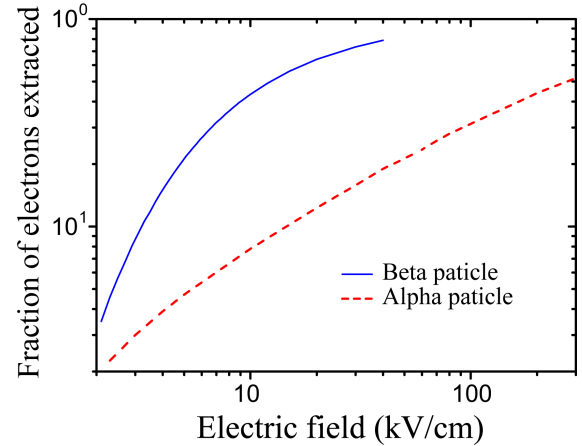


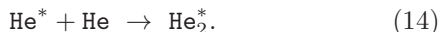
FIG. 8: (color online). Electron extraction fraction  $q$  as a function of applied electric field. The blue solid curve represents the simulated electron extraction from beta tracks by Guo *et al.* [72]. The red dashed curved represents the simulated electron extraction from alpha tracks by Ito *et al.* [73].

The mean electron-ion separation along the track of a low energy recoil He nuclei should be similar to that for beta and alpha particles. The ionization density along the He nuclei track can be estimated by  $(N_{el} + \frac{1}{3}N_{ex})/Z$ , where  $Z = \int_0^E dE'/S(E')$  is the track length of the recoil He ion. Due to the Lindhard effect, a major part of the projectile energy is lost to elastic collisions at small  $E$ . Consequently the ionization density along the track of a recoil He ion should be much lower than that along the track of an energetic alpha particle. For instance, for a 10 keV recoil He nuclei, the ions produced are on average separated by about 20 nm along the track. At lower recoil energies, the separation between ionizations becomes comparable or even larger than the mean electron-ion separation. As a consequence, the charge extraction fraction  $q$  for low energy nuclear recoils is expected to be similar to that for electron recoils. Due to the lack of experimental information, in the following analysis we assume the same  $q$  for both low energy recoil He nucleus and beta particles. The charge counts S2 for nuclear recoils and electron recoils are thus given by  $q(Y_{el} + \frac{1}{3}Y_{ex})E$  and  $q(Y_{el}^{(e)} + \frac{1}{3}Y_{ex}^{(e)})E$ , respectively. Note that the terms  $\frac{1}{3}Y_{ex}$  and  $\frac{1}{3}Y_{ex}^{(e)}$  account for the ionizations produced by

the auto-ionization of the excited He atoms.

## 2. Excitations and scintillation

Excited helium atoms can be produced in excitation collisions. For electron recoils, Sato *et al.* [66] calculated that 83% of the excited helium atoms produced in excitation collisions are in the spin-singlet states and the rest 17% are in triplet states. For low energy nuclear recoils, however, the direct excitations are nearly all to spin-singlet states [53, 62]. This is because that since the total spin is conserved, excitation to triplet states can occur only when both the recoil He and the ground state He atom are excited simultaneously to triplet states. This process requires more energy and has a lower chance to occur. The excited atoms are then quickly quenched to their lowest energy singlet and triplet states,  $\text{He}^*(2^1\text{S})$  and  $\text{He}^*(2^3\text{S})$ , and react with the ground state helium atoms of the liquid, forming excited  $\text{He}_2(A^1\Sigma_u)$  and  $\text{He}_2(a^3\Sigma_u)$  molecules



$\text{He}_2^*$  excimer molecules are also produced as a consequence of recombinations of electron-ion pairs. For geminate recombination, experiments [74] indicate that roughly 50% of the excimers that form on recombination are in excited spin-singlet states and 50% are in spin-triplet states.  $\text{He}_2^*$  molecules in highly excited singlet states can rapidly cascade to the first-excited state,  $\text{He}_2(A^1\Sigma_u)$ , and from there radiatively decay in less than 10 ns to the ground state [82],  $\text{He}_2(X^1\Sigma_g)$ , emitting ultraviolet photons in a band from 13 to 20 eV and centered at 16 eV. As a consequence, an intense prompt pulse of extreme-ultraviolet (EUV) scintillation light is released following an ionizing radiation event. These photons can pass through bulk helium and be detected since there is no absorption in helium below 20.6 eV.

The radiative decay of the triplet molecules  $\text{He}_2(a^3\Sigma_u)$  to the singlet ground state  $\text{He}_2(X^1\Sigma_g)$  is forbidden since the transition involves a spin flip. The radiative lifetime of an isolated triplet molecule  $\text{He}_2(a^3\Sigma_u)$  has been measured in liquid helium to be around 13 s [83]. The triplet molecules, resulting from both electron-ion recombination and from reaction of excited triplet atoms, diffuse out of the ionization track. They may radiatively decay, react with each other via bimolecular Penning ionization [84], or be quenched at the container walls. Experimentally, these molecules can be driven by a heat current to quench on a metal detector surface and be detected as a charge signal [85, 86].

Note that non-radiative destruction of singlet excimers by the bimolecular Penning ionization process can lead to the quenching of the prompt scintillation light. Such quenching effect has been observed for energetic alpha particles in liquid helium [74, 87]. At temperatures above 2 K, the singlet excimers can diffuse on the order of 10 nm in their 10 ns lifetime [88]. Based on the discussion

presented in the previous section, the mean separation of the excimers along the track of a low energy recoil helium can be greater than the diffusion range of the singlet excimers. The quenching of the prompt scintillation for low energy nuclear recoils should thus be small. At low temperatures, the quenching effect may be significant. However, it has been observed that even for the highly ionizing track of an energetic alpha particle, the light quenching becomes mild below about 0.6 K [87]. This is presumably due to the trapping of the excimers on quantized vortex lines that are created accompanying the energy deposition of the recoil helium [86]. Such trapping limits the motion of the excimers and hence reduces the light quenching. Lack of experimental knowledge about the decay rates at which bimolecular Penning processes occur among the different excimers, we shall not include the quenching effect in our analysis.

Based on the above discussion, the prompt scintillation photons ( $S1^{(e)}$ ) and triplet molecules ( $S3^{(e)}$ ) produced by an electron recoil event are given by

$$S1^{(e)} = E \cdot \left[ Y_{el}^{(e)} \cdot (1 - q) \cdot 50\% + Y_{ex}^{(e)} \cdot 86\% \cdot \frac{2}{3} + Y_{ex}^{(e)} \cdot 86\% \cdot \frac{1}{3} \cdot (1 - q) \right] \quad (15)$$

$$S3^{(e)} = E \cdot \left[ Y_{el}^{(e)} \cdot (1 - q) \cdot 50\% + Y_{ex}^{(e)} \cdot 14\% \cdot \frac{2}{3} + Y_{ex}^{(e)} \cdot 14\% \cdot (1 - q) \cdot \frac{1}{3} \right] \quad (16)$$

The factor  $2/3$  accounts for the fraction of the excited atoms that do not undergo autoionization. The above two formulas assume that the recombination of electron-ion pairs produced by the autoionization of singlet (or triplet) helium atoms tends to generate only singlet (or triplet) helium excimers. The justification for this assumption is that the energy of the electrons produced in the Hornbeck-Molnar process is low (less than 2 eV). These electrons do not move very far from their parent ions, hence their spin correlation with their parent ions is likely strong enough to survive the whole ionization-recombination process. As for the nuclear recoils, the  $S1^{(n)}$  and  $S3^{(n)}$  counts are given by

$$S1^{(n)} = E \cdot \left[ Y_{el} \cdot (1 - q) \cdot 50\% + Y_{ex} \cdot \frac{2}{3} + Y_{ex} \cdot \frac{1}{3} \cdot (1 - q) \right] \quad (17)$$

$$S3^{(n)} = E \cdot Y_{el} \cdot (1 - q) \cdot 50\% \quad (18)$$

Since the excited atoms are assumed to be all in singlet states for nuclear recoils, the triplet molecules are generated solely as a consequence of the recombination of charge pairs produced in direct ionization collisions.



For the readers' convenience, in table I, we summarize the formulas that we used to estimate the S1, S2, and S3 counts for both nuclear recoils and electron recoils with incident energy of  $E$ .

### C. Discrimination of nuclear recoil and electronic recoil

#### 1. Ratios of the signals from different channels

The success of a direct dark matter experiment will depend in its ability to distinguish between electron recoils and nuclear recoils. Discrimination between both types of recoils can be done by looking at the ratio of the counts from different signal channels. These ratios depend on the event type, the recoil energy, and the applied electric field. The formulas listed in table I allow us to estimate these ratios. As an example, in Fig. 9, the calculated ratios of S2/S1 and S3/S1 are shown as a function of the applied electric field for both the electron recoils and nuclear recoils with a recoil energy of 10 keV. The S2/S1 ratio for both electron recoils and nuclear recoils increases with the applied electric field. This is because at higher fields more electrons can be extracted, which enhances the S2 counts and at the meanwhile reduces the S1 counts since less electrons recombine with the ions to form singlet molecules. The difference of the S2/S1 ratio between electron recoils and nuclear recoils becomes greater at higher fields, which means that better discrimination based on S2/S1 can be achieved at higher fields.

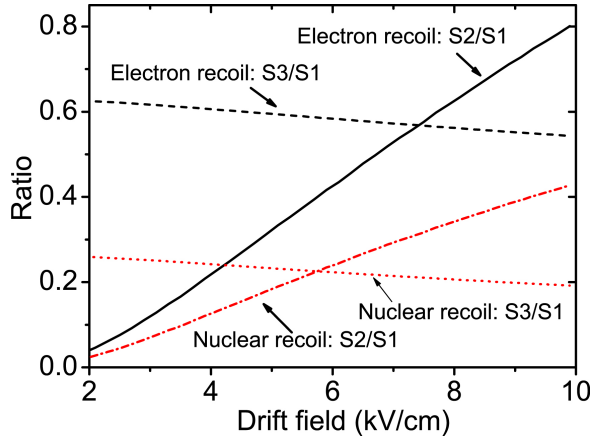


FIG. 9: (color online) The ratio of the counts from different signal channels for 10 keV nuclear recoil and electronic recoil events as a function of the applied electric field.

In Fig. 10, we show the calculated ratios of S2/S1 and S3/S1 as a function of the event energy for both electron recoils and nuclear recoils at an applied field of 8 kV/cm. Since we take the ionization and excitation yields for electron recoils to be constants, the S2/S1 and S3/S1 ratios for electrons recoils are independent of the recoil energy.

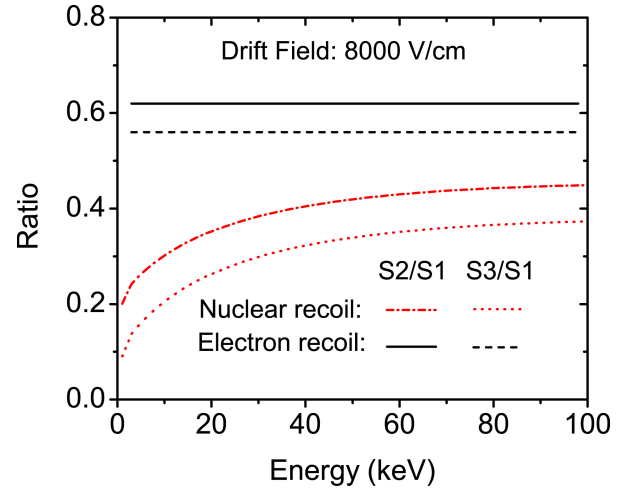


FIG. 10: (color online) The ratio of the counts between different signal channels for nuclear recoil and electronic recoil events as a function of the event energy. The applied electric field is 8 kV/cm.

For nuclear recoils, both the S2/S1 and S3/S2 ratios decrease with decreasing recoil energy. Note that the ratios evaluated here are based on the calculated average counts from the different signal channels. In real experiment, there always exist number uncertainties of the counts. At low recoil energies where the counts are small, the relative uncertainties of the counts as well as the ratios of the counts between different channels become large, which limits the discrimination of the two types of recoils. For helium detector, as we can see from Fig. 10, the S2/S1 and S3/S1 curves for nuclear recoils bend away from those for electron recoils, which compensates the effect due to count uncertainty. As we shall show later, excellent event discrimination can still be achieved even down to a few keV energy regime.

#### 2. Scintillation efficiency factor

The quantities that can be measured experimentally for a recoil event are the counts from the different signal channels. One can plot, for instance, the S2/S1 ratio against the S1 counts. However, the conversion between S1 counts to the event energy is different for electron recoils and nuclear recoils. For electron recoils, the event energy is proportional to the S1 counts, since the ionization and the excitation yields are taken to be constant. For nuclear recoils, such conversion is nonlinear. The effective scintillation efficiency  $L_{eff}$  describes the difference between the amount of energy measured in the detector between both types of recoils. In the notation used in the field, the keV electron equivalent scale (keVee) is used to quantify a measured signal in terms of the energy of an electron recoil that would be required to generate it. Similarly the keVr scale is used for nuclear recoil events. For a nuclear recoil of energy  $E_r$ , the electron recoil event

TABLE I: The yields of prompt scintillation (S1), charge (S2), and  $\text{He}_2^*$  triplet molecules (S3) for nuclear recoils and electron recoils with incident energy of  $E$  in liquid helium.

	Nuclear recoils	Electron recoils
S1	$E \cdot [0.5 \cdot Y_{el} \cdot (1 - q) + 0.67 \cdot Y_{ex} + 0.33 \cdot Y_{ex} \cdot (1 - q)]$	$E \cdot [0.5 \cdot Y_{el}^{(e)} \cdot (1 - q) + 0.57 \cdot Y_{ex}^{(e)} + 0.29 \cdot Y_{ex}^{(e)} \cdot (1 - q)]$
S2	$E \cdot (Y_{el} + 0.33 \cdot Y_{ex}) \cdot q$	$E \cdot (Y_{el}^{(e)} + 0.33 \cdot Y_{ex}^{(e)}) \cdot q$
S3	$E \cdot Y_{el} \cdot 0.5 \cdot (1 - q)$	$E \cdot [0.5 \cdot Y_{el}^{(e)} \cdot (1 - q) + 0.093 \cdot Y_{ex}^{(e)} + 0.047 \cdot Y_{ex}^{(e)} \cdot (1 - q)]$

that would produce an equivalent S1 signal is given by

$$E_e(\text{keVee}) = L_{eff} \times E_r(\text{keVr}). \quad (19)$$

By definition  $L_{eff}$  is the nuclear recoil scintillation efficiency relative to that of an electron recoil of the same energy at zero field. Experimentally, the conversion between S1 and the electron equivalent scale keVee can be established using gamma line sources, for example the  $^{57}\text{Co}$  122 keV line. The nuclear recoil response as a function of energy can be established using neutron scattering, either in a mono-energetic neutron scattering experiment, or by using a neutron source with a broad energy distribution and comparing the observed shape of the nuclear recoil spectrum with detailed Monte Carlo simulations. Using the formulas listed in Table I, we can estimate the  $L_{eff}$  by calculating the ratio of the energies of the two types of recoil events that give the same S1 counts. The result is shown in Fig. 11.

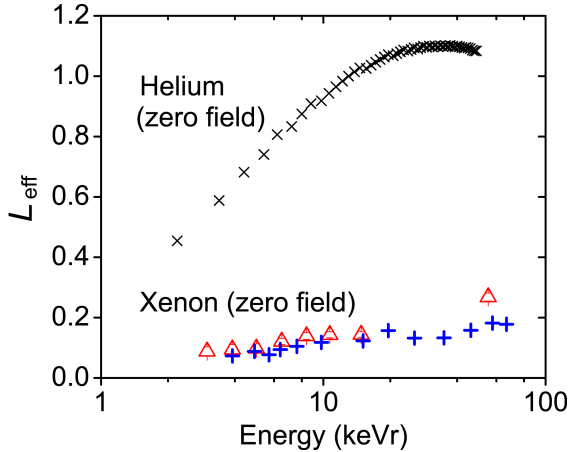


FIG. 11: (color online) The effective quenching factor  $L_{eff}$  as a function of the recoil event energy. The  $\times$  represents the calculated  $L_{eff}$  for helium under zero applied electric field. The measured data for liquid Xenon by G. Plante *et al.* [89] ( $\Delta$ ) and by A. Manzur *et al.* [90] (+) are also shown.

The event discrimination ability of a detector drops drastically below a certain threshold S1 counts. For a given energy threshold in keVee scale, a detector with a higher  $L_{eff}$  has lower nuclear recoil energy threshold, hence would be sensitive to low energy WIMPs. In Fig. 11, we also show the experimentally measured  $L_{eff}$  data for liquid Xenon [89, 90]. In the low energy regime of a few keV, Xenon-based detector only has a  $L_{eff}$  of

less than 0.1 while helium detector has a  $L_{eff}$  above 0.4. So while liquid helium has substantially lower scintillation yield for electron recoils, this is unlikely to be the case for nuclear recoils.

### 3. Rejection power

The uncertainty of the signal counts limits the discrimination between the nuclear recoils and the electron recoils at low energies. To study this effect, we performed a Monte Carlo simulation. For a given recoil energy  $E$  in electron equivalent energy scale, we randomly generate S1 and S2 counts for a nuclear recoil event and an electron recoil event, assuming a Poisson distribution of the counts with mean count values given by the formulas listed in Table I. In each trial, the ratios of S2/S1 for a nuclear recoil and for an electronic recoil are evaluated and represented by a red dot and a black dot in the S2/S1 versus  $E$  plot.  $10^7$  trials are carried out for each energy. An example is shown in Fig. 12. To match with real experiments, we assume that only 20% of the scintillation photons (S1) are collected (typical for a two-phase detector as we shall discuss later), and that all the extracted electrons (S2) under the applied drift electric field can be detected. A clear separation can be seen between the electron recoil band and the nuclear recoil band, a necessary criterion for any direct dark matter experiment. At low energies, the two bands overlap due to the large scattering of the S2/S1 value. This large scattering is caused by the large relative uncertainty of the counts when their mean values of the Poisson distributions are small.

To calculate the rejection power, we divide the two bands in energy slices. We select the lower half of the nuclear recoil band as our WIMP region of interest. At low energies it is crucial to know what percentage of the electronic recoil band leak into the lower 50% nuclear recoil band. The rejection power (or sometimes called discrimination power) is found as the fraction of electronic recoil events below the nuclear recoil centroid. A full description on this method has been given by A. Manalaysay [91]. In Fig 13, we show the calculated rejection power as a function of event energy in keVr scale at several applied electric fields and with different S1 collection efficiencies. At low energies, the ability to distinguish electron and nuclear recoils is degraded because of the lack of charge and light signal. But above a few keV, discrimination power is predicted to improve considerably,

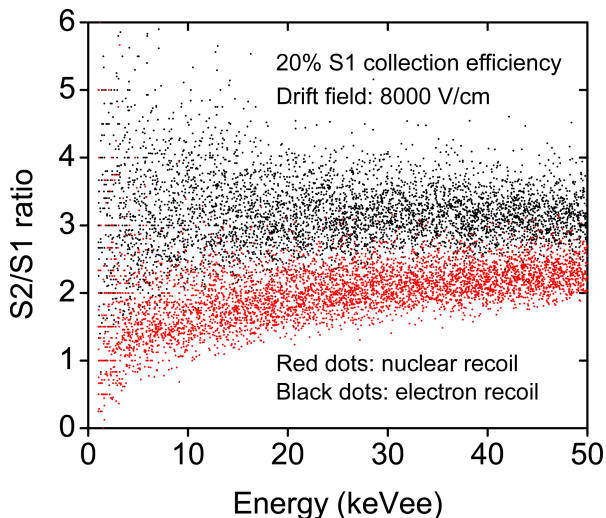


FIG. 12: (color online) Monte Carlo simulation of S1/S2 ratio for nuclear recoils (red dots) and electronic recoils (black dots). The S1 scintillation light collection efficiency is assumed to be 20%. The applied electric field is 8 kV/cm. The event energy is in the keV electron equivalent energy scale (keVee).

and this should allow for low-background operation and a sensitive WIMP search. The discrimination is better at higher fields or with higher S1 collection efficiency. We considered fields up to 40 kV/cm. It has been shown that such high fields can be readily applied in liquid helium [73]. Indeed, the design electric field value of the Spallation Neutron Source (SNS) neutron EDM experiment is 50 kV/cm [92–94]. As we shall discuss later, for a single-phase helium detector operated at very low temperatures, sensitive bolometers immersed in liquid helium may be used to read out the light and the charge signals. In this case, 80% S1 collection may be possible with the detector inner surface being covered by bolometer arrays. Note that the rejection power analysis is based on the the charge extraction curve shown in Fig. 8. The actual charge extraction at a given field could be higher, especially at low temperatures where the ionized electrons can stray away from field lines [72]. Considering this factor, the actual rejection power could be better than the results shown in Fig 13.

### III. HELIUM-BASED DETECTOR

For dark matter detection, we propose to detect both prompt scintillation and charge in liquid helium-4, using a time projection chamber design. This is essentially the same approach used in Ar and Xe detectors [95–97], which has proven to be very effective, providing excellent position resolution and gamma ray discrimination. Based on the readout schemes for the light and charge signals, we discuss two proposals for a liquid-helium-based dark matter detector. One proposal is to operate the detec-

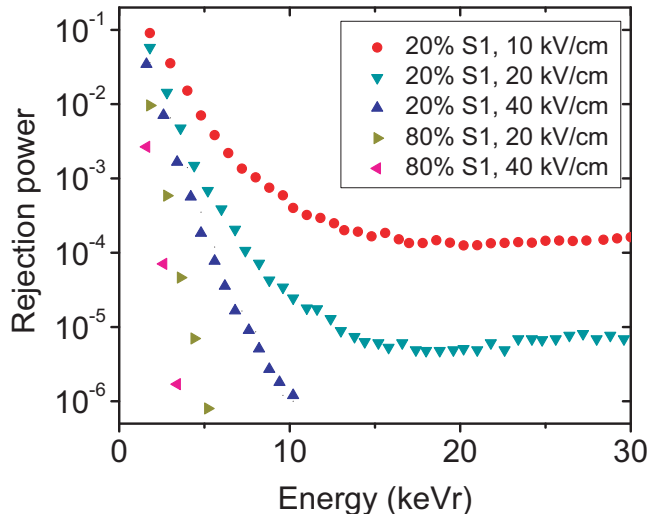


FIG. 13: (color online) Calculated rejection power for a helium detector as a function of event energy in keVr scale.

tor at high temperature regime ( $\sim 3$  K) using photomultiplier tube arrays for signal readout, and the second proposal is to operate the detector at low temperatures ( $\sim 100$  mK) using bolometer arrays for signal readout.

#### A. High temperature operation scheme

Operating a helium detector at relatively high temperatures is favored in economy since such a detector does not require complicated large-scale dilution refrigeration system. At high temperatures where the helium vapor density is high, some existing technologies for charge signal amplification may be readily applied to the helium detector, such as the proportional scintillation in a two-phase chamber that has been used in Argon, Krypton, and Xenon detectors [95–98], or the electron avalanche in a Gas Electron Multiplier (GEM) [99–101].

A conceptual schematic of a two-phase helium-based time projection chamber is shown in Fig. 14. Ionizing radiation events in liquid helium produce both prompt scintillation light (S1) and ionizations. A drift electric field can be maintained between the anode and the cathode. Some ionized electrons can be extracted into the gas phase and caused to emit 16 eV EUV photons (S2) by a strong field in the vapor. The anode and cathode may be a transparent material coated with Indium Tin Oxide such as recently demonstrated in the DarkSide-10 experiment [102], so produce a uniform proportional scintillation field and eliminate liquid helium scattering events below the cathode. To detect the EUV photons, as is typical for scintillation detection in liquid argon, liquid neon, and liquid helium, the inner surface of the chamber windows and the transparent electrodes can be coated with tetraphenyl butadiene (TPB) wavelength shifter. The

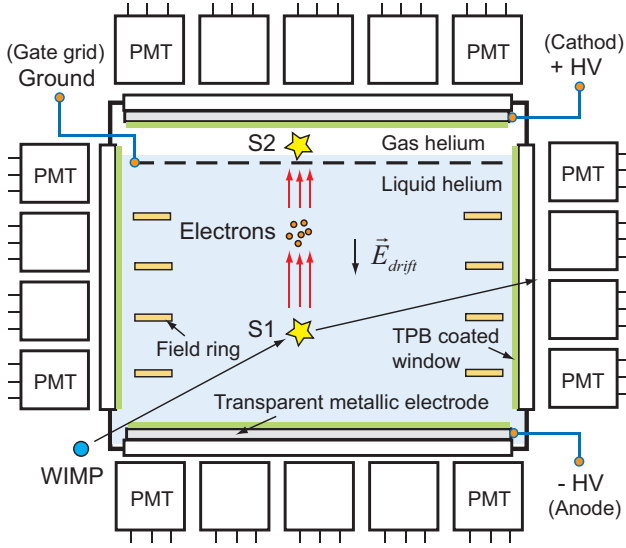


FIG. 14: (color online). A schematic of a two-phase helium-based dark matter detector.

EUV scintillation light is converted to the visible on the TPB coating, which has approximately 100% photon-to-photon conversion efficiency at the helium scintillation wavelength of 80 nm [33]. Photomultiplier tube (PMT) array placed outside the helium chamber can be used to detect the converted photons. S1 light detection efficiency of about 20% may be expected in such a detector, similar to that measured by the DarkSide collaboration [102], which recently demonstrated a zero-field signal yield of 9.1 photoelectrons/keVee in a two-phase liquid argon detector. With time projection readout, the time between the S1 and S2 signals indicates the depth ( $z$ ) of the event, while the hit pattern in the top array of photomultipliers gives the  $x - y$  position of the event. This allows determination of a low-background central fiducial volume, which is used for the dark matter search. Events close to chamber surface may be discarded, and the S2/S1 ratio provides discrimination power against gamma ray background. Any gamma ray or neutron events that cause multiple scatters will generate multiple S2 signals, and these may also be discarded.

The extracted electrons moving in helium vapor undergo collisions with helium atoms. Due to their very small mass the electrons can give up almost no energy to the helium atoms in the course of elastic collisions. When the kinetic energy of the electrons builds up over a few mean free paths to exceed the excitation threshold ( $\sim 20$  eV) of helium atoms, inelastic collisions between the electrons and the helium atoms, which lead to the production of excited helium atoms, can occur. The excited helium atoms in spin-singlet states can react with surrounding helium atoms and decay to the ground state by emitting 16 eV EUV photons (S2). The S2 strength increases with the applied field. However, when the electric field in vapor is too strong, the electron energy can exceed the ionization threshold ( $\sim 24.6$  eV) of

helium atoms. In this situation, charge multiplication in gas occurs, and eventually avalanche breakdown can take place. Given the premium on high electric field for getting good event discrimination, it is advantageous to operate the detector at a field in the vapor only slightly below the breakdown field. The breakdown voltage  $V_{bd}$  of helium gas in a uniform field generated by a pair of electrodes separated by a distance  $d$  is given by the Paschen's law [103]

$$V_{bd} = \frac{A \cdot \rho \cdot d}{\ln(\rho \cdot d) + B} \quad (20)$$

where  $\rho$  is gas density.  $A$  and  $B$  are experimentally determined constants. Some available experimental data of the breakdown voltage for helium gas are shown in Fig. 15 (a) [104, 105]. The solid curve represents a typical Paschen's curve for helium gas obtained by fitting the experimental data using Eq. 20 [105, 106].

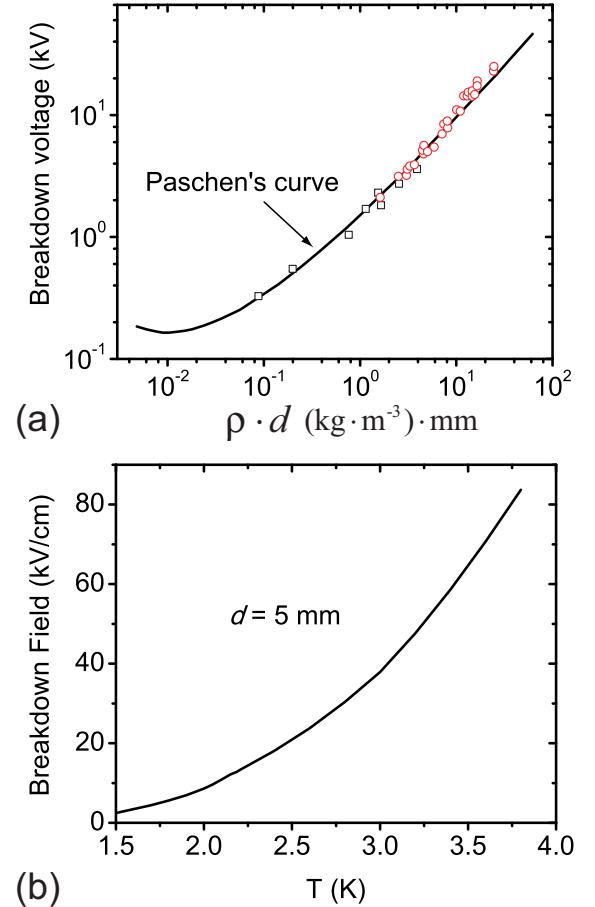


FIG. 15: (color online). (a) The dielectric breakdown voltage in helium gas as a function of the product of the gas density  $\rho$  and the electrode separation  $d$ . The red circles ( $\circ$ ) and the black squares ( $\square$ ) are experimental data from Ref. [104] and Ref. [105], respectively. The solid curve represents the Paschen's curve obtained by fitting the experimental data [105, 106]. (b) The dielectric breakdown field for saturated helium vapor as a function of temperature.



For saturated helium vapor in a two-phase helium detector, the gas density as a function of temperature is known [107]. We can thus use the Paschen's curve to calculate the breakdown field for a two-phase helium detector as a function of the operation temperature for a given electrode separation  $d$  in the vapor. In Fig. 15 (b), the calculated breakdown field at  $d = 5$  mm is shown. As we can see, the breakdown field increases drastically with temperature due to the increased vapor density. At 3.2 K, the breakdown field is about 40 kV/cm. Under a drift field  $E_{\text{drift}}$  that is close to this breakdown field, good event discrimination power is expected.

The drift speed of the electrons  $v$  in liquid helium is given by  $v = \mu E_{\text{drift}}$ , where  $\mu$  is the electron mobility in the liquid. Electrons drift much slower in liquid helium than in liquid xenon and liquid argon due to the small  $\mu$  associated with the bubble state in helium. Based on the known mobility of the electrons in helium [108], their drift velocity under a field close to the vapor breakdown field as given in Fig. 15 (b) can be calculated. The result is shown in Fig. 16. The electron speed drops with increasing temperature below the lambda point ( $\sim 2.17$  K), which is due to the steep drop of the electron mobility. Above the lambda point,  $\mu$  decreases slowly with increasing temperature, and the electron speed rises steadily as the breakdown field increases. At 3.2 K, the electron speed is about 10 m/s. For a 10-liter sensitive volume, if we take the distance from the bottom electrode to the liquid/gas interface to be 20 cm, the maximum delay time between S1 and S2 will be about 20 ms. For a well shielded detector, event pileup should be well below the level that would cause mismatching of S1 and S2 signals.

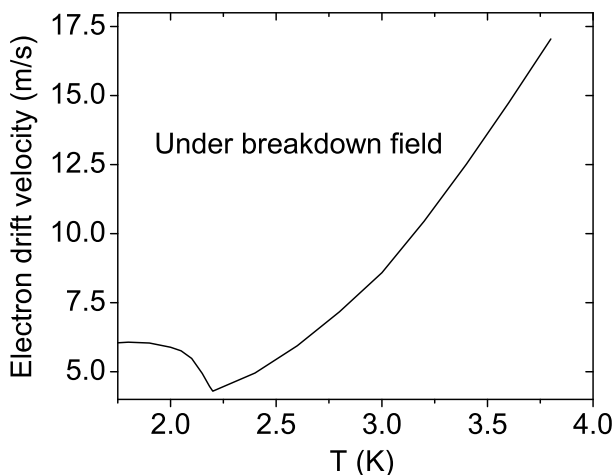


FIG. 16: (color online). The electron drift velocity in liquid helium as a function of the temperature under a drift field that is close to the breakdown field for saturated helium vapor.

Alternatively one may detect the extracted electrons using Gas Electron Multipliers (GEMs) or Thick Gas Electron Multipliers (THGEMs) [99–101]. Detecting

electrons using GEMs has already been studied experimentally by the “e-bubble” collaboration [109, 110]. A disadvantage of the GEM is that it gives poorer energy resolution than proportional scintillation since it relies on a breakdown for electron gain. However, because of the slow electron drift speed, the electrons will arrive at the GEM one at a time, easily distinguishable due to the excellent GEM timing resolution. We may operate the GEM in a single electron detection mode, counting single electron pulses instead of using the pulse sizes to determine the event energy. Note that it was shown that in ultrapure helium gas GEM can operate only at charge gain close to unity [111, 112]. However, during the avalanche development, excited helium atoms and molecules are produced. The decay of these electronic excitations leads to the emission of 16 eV photons. Instead of detecting the charge produced in the GEM, we may detect these photons with arrays of PMTs. At the same time the GEM (or stack of GEMs) could also be used to amplify the prompt scintillation signal. The side of the GEM facing the liquid could be coated with Cesium Iodide (CsI) [113] or other photocathode material so as to be sensitive to the prompt scintillation light. Furthermore, the extracted electrons may also be detected via electroluminescence produced under very high ( $\sim 1$ -10 MV/cm) fields on the surface of thin wires or a GEM immersed in liquid helium. Such electroluminescence has already been observed in liquid Ar [114] and liquid Xe [14]. This could allow electrons to be individually detected, while not subjecting gaseous helium to a strong electric field.

## B. Low temperature operation scheme

At very low temperatures (e.g. 100 mK), calorimetric sensors with small heat capacity can be used for particle/photon detection with remarkable sensitivity and low threshold. A significant advantage of using calorimetric sensors is that one could in principle cover all the inner surface of the detector with calorimetric sensor arrays, while not being limited by the 20–30% quantum efficiency typical of photocathodes. S1 light collection efficiency approaching 100% might be achieved, which would improve the rejection power of the detector. At low helium temperatures, the thermal coupling between the calorimetric sensors and the liquid helium is weak, enabling them to be immersed in the liquid helium without losing much thermal signal to the bath.

The field of low temperature bolometers is developing rapidly. The types of temperature sensors most commonly used are neutron-transmutation doped (NTD) Germanium thermistors, and superconducting transition edge sensors (TES) [115, 116]. The electric conductivity of NTD sensors strongly depends upon the temperature, with typically resistance of  $1 \sim 100$  M $\Omega$  at low temperatures. NTD thermistors are easy to use because they can be operated with conventional electronics. Mass production is also possible for the NTD sensors. A TES is a

superconducting strip operating at the temperature of its superconducting-normal transition. The resistance in the normal state is usually  $10\text{ m}\Omega \sim 1\Omega$ , and the temperature dependence of the resistance can be very large at the transition. Recent developments include not only improvements in single TES's, but also large arrays of TES's and techniques for multiplexing them. For this dark matter application, especially promising are non-equilibrium detectors, in which interactions produce quasiparticles in a superconducting strip, which can be then collected in a TES and detected [117]. Another possible choice is metallic magnetic calorimeters (MMC) [118–120]. MMCs are based upon the use of magnetic sensors to measure very small temperature changes resulting from the absorption of energy by energetic photons. Instead of measuring the resistance of a sensor such as an NTD or a TES, an MMC measures the change of magnetization of paramagnetic ions in a metallic host [121, 122]. The internal thermalization time of MMCs is very fast, within a microsecond.

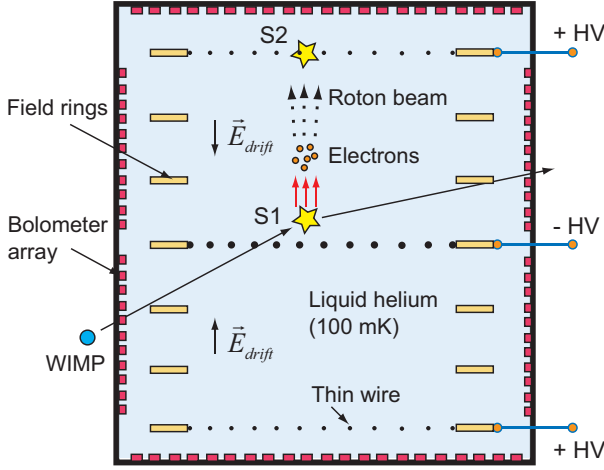


FIG. 17: (color online). A schematic of a single-phase helium detector operated at mK temperatures.

A conceptual schematic of a calorimeter-based single-phase helium time projection chamber is shown in Fig. 17. The prompt 16 eV photons produced by a recoil event hit the bolometer arrays and deposit their energy in the sensors which give rise to the S1 signal. At low temperatures, bolometers may be made sensitive enough to allow the detection of individual photons [117, 120]. To extract the ionized electrons, three electrodes are arranged in a way to drive the electrons toward either the top or the bottom electrode. Since all the electrodes are immersed in liquid helium, high voltages ( $\sim \pm 100\text{ kV}$ ) can be applied to them. The drift field with the shown electrode arrangement can be made as high as a few tens of kV/cm, which helps to improve the rejection power of the detector. To amplify and detect the charge signal, both the top and the bottom electrodes are made of thin wire arrays. The extracted electrons drifting towards these thin wires may produce electroluminescence

as they approach the wire surface. These photons (S2) can be detected by the same bolometer arrays. Again, event position reconstruction can be made based on the delay between S1 and S2, and the hit pattern on the top (or bottom) bolometer array.

Note that the mobility of electron bubbles in liquid helium increases drastically with decreasing temperature. Under saturated vapor pressure, if the velocity of the electrons exceeds a threshold velocity of the order of 40 m/s, quantized vortex rings are nucleated. The electrons can get stuck on them, and the charged vortex ring moves through the liquid as a single entity. A striking feature of the electron-ring complex is that its velocity decreases with increasing energy [123]. When a strong drift field (a few kV/cm) is applied, the velocity of the charged vortex rings can be as low as on the order of 1 m/s [124]. However, it has been shown that at low temperatures when isotropically purified helium is pressurized to above 15 bar, electrons can be driven at a speed close to or higher than the Landau velocity ( $\sim 50\text{ m/s}$ ). Instead of nucleating vortex rings, the electrons spontaneously emit roton pairs [125–127]. The rate of roton emission depends on the field strength. Furthermore, it has been shown that when the electron speed is not too much higher than the Landau velocity, the majority of the emitted rotons tend to have momentum aligned in the same direction with the electron velocity [128]. A roton beam is formed accompanying every extracted electrons. Note that rotons in the  $R^+$  branch move along the electron velocity direction due to their positive effective mass, while  $R^-$  rotons are emitted in the opposite direction since their effective mass is negative in helium [129]. Despite the low transmission coefficient of the roton energy across the liquid-solid interface at low temperatures, a fraction of the roton energy can nevertheless transmit into the bolometers and be detected [130]. Detecting the rotons provides a unique way for charge signal amplification and detection, with potentially hundreds of keV of roton signal produced by each drifted electron. Operation at pressure  $> 15\text{ bar}$ , as required in this approach, may also be advantageous for maintaining higher drift field by suppressing gas bubble formation.

Note that in the initial proposal by Lanou *et al.* [30], the idea of charge signal amplification via roton/vortex generation was briefly mentioned. It was proposed that event discrimination might be achieved based on the ratio of prompt rotons accompanying the initial recoil deposition to the delayed rotons from the drifted charge. Due to the low transmission of roton energy into the bolometer surface, detecting the prompt rotons for low energy recoils can be quite challenging. Nevertheless, if detection of prompt rotons and phonons could be accomplished for very low energy nuclear recoil events, search for extremely light WIMPs may be conducted. At very low energies, ionization is strongly suppressed for nuclear recoil events, and even a single electron from an electron recoil event would produce a large roton signal, allowing electron recoil backgrounds to be vetoed. In addition,

the roton/phonon ratio may be different for nuclear and electron recoils, allowing electron recoil backgrounds to be discriminated by bolometer pulse shape.

It is worthwhile mentioning that at low temperatures, metastable helium molecules in triplet state can drift at a speed of a few meters per second [86]. When these molecules collide on the bolometer surface, they undergo non-radiative quenching and release over 10 eV of energy depending on the material of the impinged surface. A significant amount of this energy will be deposited into the calorimetric sensor, which may allow us to detect the molecule signal (S3). A combined analysis of S2/S1 and S3/S1 ratios may further improve the rejection power of the detector.

#### IV. SENSITIVITY

In any direct dark matter detection scheme, the primary requirement is the strong reduction of radioactive backgrounds. The approaches described above are designed to enable this, since liquid helium may readily be purified of impurities, and because the ratios of signal channels may be used to identify gammas and betas on an event-by-event basis.

Internal backgrounds (due to radioactive impurities within the target material) are particularly straightforward to eliminate in liquid helium. Like other noble gases, helium is readily purified with heated getters to remove any chemically reactive species, which includes anything that is not a noble gas. In addition, helium has no long-lived radioactive isotopes and therefore has no intrinsic backgrounds, unlike argon and krypton which contain the beta emitters  $^{39}\text{Ar}$  and  $^{85}\text{Kr}$ . Activated charcoal adsorber may then be used to remove all other radioactive noble gases (e.g. radioactive argon, krypton, and radon), since all other noble gases have larger polarizabilities and masses, leading to larger binding energies to charcoal and substantially larger adsorption coefficients [131, 132]. Getters and charcoal may be used to purify the helium after it is transported underground. Any remaining impurities will fall out of liquid helium and stick to plumbing and detector walls, and any beta, alpha, or nuclear recoil background due to these impurities may be removed through position reconstruction.

External backgrounds may be reduced through shielding, careful detector materials selection, and event discrimination. The dominant background in this experiment is expected to arise from gamma rays that Compton scatter in the helium and produce low-energy events that could be confused with dark matter particles. This gamma ray Compton scattering background tends to be flat with energy at low energies, and a typical Compton scattering background rate for a shielded dark matter experiment is about 1 event/keVee/kg/day, though this may be reduced further with special care given to shielding and detector materials. Neutron backgrounds are typically well subdominant to gamma rays, for most

detector construction materials. Radon daughter backgrounds on inner detector surfaces can be troublesome, but are eliminated in this scheme through the excellent position reconstruction inherent to noble liquid time projection chambers.

With gamma rays generating the dominant background, it is crucial to have excellent electron recoil versus nuclear recoil discrimination. From the quantitative estimates described in Section II above, we have good confidence that liquid helium will indeed provide excellent discrimination power. In addition, the helium detector may be surrounded with a veto detector that is sensitive to gamma rays. Using organic scintillator, liquid xenon, or liquid argon as detector materials, such a veto may be used to efficiently tag gamma rays that small-angle-scatter in the helium fiducial volume, produce low energy events, and escape. Efficiencies of 90-98% may be expected, as predicted for the DarkSide and LUX-ZEPLIN experiments [102, 133].

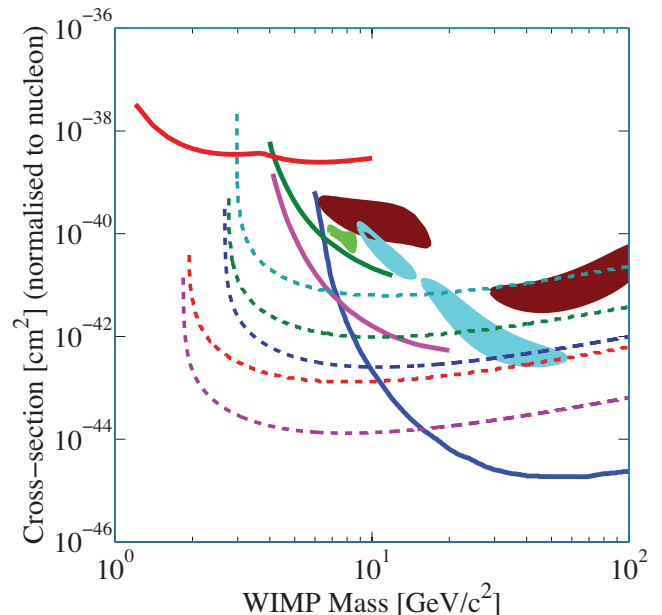


FIG. 18: (color online). Spin-independent WIMP exclusion curves (solid lines), potential WIMP signals (solid regions), and projected liquid helium 90% sensitivity curves (dashed lines) in the region of 1-100 GeV WIMP mass. Exclusion curves include DAMIC in red [135], CDMS-II in green [10], XENON10 in magenta [12], and XENON100 in blue [14]. Potential WIMP signals include DAMA in red [136], CRESST in light blue [17], and CoGeNT in green [16]. Projected liquid helium sensitivities for different detector parameters are shown as dashed lines, including light blue (10 kV/cm, 20% S1 collection, 4.8 keV threshold), green (20 kV/cm, 20% S1 collection, 4.4 keV threshold), blue (40 kV/cm, 20% S1 collection, 4.2 keV threshold), red (20 kV/cm, 80% S1 collection, 2.8 keV threshold), and magenta (40 kV/cm, 80% S1 collection, 2.6 keV threshold). Predicted limits assume an electron recoil background of 1 event/keVee/kg/day and a 95% efficient gamma ray veto.

As explained in section I, a useful figure of merit for light WIMP searches is (nuclear mass) $\times$ (energy threshold), which must be minimized to get the best light WIMP sensitivity. In the case of liquid helium, this must be balanced with the background reduction achieved through discrimination of electron recoil events, which improves with higher energy. Given helium's large predicted nuclear recoil signals and excellent discrimination, we expect an energy threshold of about 4-5 keV with photomultiplier readout, potentially reducible to 1-3 keV with bolometric readout. The low nuclear mass of helium then gives access to very low WIMP masses, while still having significant background reduction through discrimination.

While liquid helium will not provide significant self-shielding against gamma rays and neutrons (a significant background rejection method in LXe and LAr detectors), a plausible background rate of  $10^{-3}$  events/day/keVee/kg after discrimination will allow excellent sensitivity to light WIMPs, for which current experimental sensitivities are relatively weak. A detailed discussion of the background of a helium detector designed for the HERON project was given by Huang *et al.* [134]. For a 1 kg helium fiducial mass, 20% light collection, a 20 kV/cm drift field, an energy threshold of 4.8 keV, 300 days of operation, and a 95% efficient gamma ray veto, one background event is predicted, with a WIMP-nucleon cross-section sensitivity of  $10^{-42}$  cm<sup>2</sup> at 5 GeV, the dark matter mass predicted by asymmetric dark matter models. Sensitivity may be improved further with higher drift fields, more efficient light collection, and

larger exposure, potentially reaching  $10^{-44}$  cm<sup>2</sup> or better between 2-20 GeV. Some predicted light WIMP sensitivities are summarized above in Figure 18.

## V. CONCLUSION

We conclude that liquid helium is an intriguing material for the direct detection of light WIMPs, as it combines multiple signal channels, comparatively large signals for nuclear recoils, a low target mass, and the capacity for electron recoil discrimination. In the detector schemes proposed here, a high electric field is used to extract electrons from nuclear recoil tracks, allowing a sizable charge signal, time projection chamber readout, and good position resolution. Before dark matter experiments can be performed with this technology, a method of detecting single electrons in liquid superfluid helium must be demonstrated. In addition, detailed measurements must be done of the nuclear and electron recoil signal and discrimination efficiency at low energies.

## Acknowledgments

We thank R.E. Lanou, D. Hooper, D. Prober, T.M. Ito, G.M. Seidel, and A. Buzulutskov for valuable discussions and comments, and D. Klemme for her assistance in preparation of this manuscript.

- 
- [1] D. N. Schramm, Proc. Natl. Acad. Sci, **95**, 42-46 (1998).
  - [2] W. Hu, Astrophys. J. Lett. **557**, L79 (2001).
  - [3] M. Tegmark, *et al.*, [SDSS Collaboration], Astrophys. J. **606**, 702 (2004).
  - [4] Y. Mellier, Annu. Rev. Astron. Astrophys., **37**, 127-189 (1999).
  - [5] M.W. Goodman and E. Witten, Phys. Rev. **D 31**, 3059 (1985).
  - [6] G. Jungman, M. Kamionkowski, and K. Griest, Phys. Rept. **267**, 195 (1996).
  - [7] J. Giedt, A. W. Thomas and R. D. Young, Phys. Rev. Lett. **103**, 201802 (2009).
  - [8] H. Goldberg, Phys. Rev. Lett. **50**, 1419 (1983).
  - [9] J.R. Ellis, J.S. Hagelin, D.V. Nanopoulos, K.A. Olive and M. Srednicki, Nucl. Phys. **B 238**, 453 (1984).
  - [10] [CDMS-lite] Z. Ahmed, *et al.*, Phys. Rev. Lett. **106**, 131302 (2011); Z. Ahmed, *et al.*, Phys. Rev. Lett. **102**, 011301 (2009).
  - [11] D. Akimov, *et al.*, Phys. Lett. **B 692**, 180 (2010).
  - [12] [XENON10] J. Angle, *et al.*, Phys. Rev. Lett. **107**, 051301 (2011).
  - [13] E. Aprile, *et al.*, Phys. Rev. Lett. **105**, 131302 (2010).
  - [14] [XENON100] E. Aprile, *et al.*, arXiv:1207.5988.
  - [15] R. Bernabei, *et al.*, Eur. Phys. J. **C 67**, 39 (2010).
  - [16] [COGENT] C.E. Aalseth, *et al.*, Phys. Rev. Lett. **106**, 131301 (2011); C.E. Aalseth, *et al.*, arXiv:1106.0650.
  - [17] G. Angloher, *et al.*, arXiv:1109.0702.
  - [18] D. Hooper, arXiv:1201.1313.
  - [19] A. Bottino, N. Fornengo and S. Scopel, Phys. Rev. **D 67**, 063519 (2003); A. Bottino, F. Donato, N. Fornengo, S. Scopel, Phys. Rev. **D 69**, 037302 (2004); J.F. Gunion, D. Hooper and B. McElrath, Phys. Rev. **D 73**, 015011 (2006); A. Bottino, F. Donato, N. Fornengo and S. Scopel, Phys. Rev. **D 78**, 083520 (2008); A. Bottino, F. Donato, N. Fornengo and S. Scopel, Phys. Rev. **D 77**, 015002 (2008); A. Bottino, F. Donato, N. Fornengo and S. Scopel, Phys. Rev. **D 81**, 107302 (2010); J.F. Gunion, A.V. Belikov, and D. Hooper, arXiv:1009.2555.
  - [20] S. Nussinov, Phys. Lett. **B 165**, 55 (1985); D. B. Kaplan, Phys. Rev. Lett. **68**, 741 (1992), D. E. Kaplan, M. A. Luty, and K. M. Zurek, Phys. Rev. **D 79**, 115016 (2009); J. Shelton and K. Zurek, arXiv:1008.1997; A. Falkowski, J. T. Ruderman, and T. Volansky, JHEP **05**, 106 (2011).
  - [21] J.L. Feng and J. Kumar, Phys. Rev. Lett. **101**, 231301 (2008); J. Feng, J. Kumar, and L. Strigari, Phys. Lett. **B 670**, 37 (2008).
  - [22] C.P. Burgess, M. Pospelov, and T. ter Veldhuis, Nucl. Phys. **B 619**, 709 (2001); S. Andreas, T. Hambye, and M.H.G. Tytgat, J. Cosmol. Astropart. Phys. **0810**, 034 (2008); Y.G. Kim and S. Shin, J. High Energy Phys. **0905**, 036 (2009).



- [23] B. Holdom, Phys. Lett. **B 166**, 196 (1986); D.P. Finkbeiner and N. Weiner, Phys. Rev. **D 76**, 083519 (2007); N. Arkani-Hamed and N. Weiner, J. High Energy Phys. **12**, 104 (2008); D. Hooper and K.M. Zurek, Phys. Rev. **D 77**, 087302 (2008); M. Pospelov, A. Ritz, and M.B. Voloshin, Phys. Lett. **B 662**, 53 (2008); K.M. Zurek, Phys. Rev. **D 79**, 115002 (2009); N. Arkani-Hamed, D.P. Finkbeiner, T.R. Slatyer, and N. Weiner, Phys. Rev. **D 79**, 015014 (2009); C. Cheung, J.T. Ruderman, L.-T. Wang, and I. Yavin, Phys. Rev. **D 80**, 035008 (2009); M. Pospelov and A. Ritz, Phys. Lett. **B 671**, 391 (2009); R. Essig, J. Kaplan, P. Schuster, and N. Toro, arXiv:1004.0691; D. Hooper, N. Weiner, and W. Xue, arXiv:1206.2929.
- [24] R. Foot, Int. J. Mod. Phys. **D 13**, 2161 (2004); R. Foot, Phys. Rev. **D 78**, 043529 (2008).
- [25] G. Giesen, *et al.*, arXiv:1209.0247.
- [26] S. Chatrchyan, *et al.*, (CMS Collaboration), Phys. Rev. Lett. **108**, 261803 (2012); ATLAS Collaboration, arXiv:1210.4491.
- [27] M. Ackermann, *et al.*, (The Fermi-LAT Collaboration), Phys. Rev. Lett. **107**, 241302 (2011); A. Geringer-Sameth and S.M. Koushiappas, Phys. Rev. Lett. **107**, 241303 (2011).
- [28] J.D. Lewin and P.F. Smith, Astroparticle Physics **6**, 87 (1996).
- [29] R.E. Lanou, H.J. Maris, and G.M. Seidel, Phys. Rev. Lett. **58**, 2498 (1987); S.R. Bandler, C. Enss, G. Goldhaber, R.E. Lanou, H.J. Maris, T. More, F.S. Porter, and G.M. Seidel, J. Low Temp. Phys. **93**, 785 (1993).
- [30] R.E. Lanou, H.J. Maris, and G.M. Seidel, Proc. XXIII Ren. de Moriond, Editions Frontieres, 79-83 (1988).
- [31] J. Adams, *et al.*, Proc. XXXIst Moriond Conference, Les Arcs (France), 14-27 (1996).
- [32] D.I. Bradley, *et al.*, Nucl. Instrum. Methods **A 370**, 141 (1996); C.B. Winkelmann, *et al.*, Nucl. Instrum. Methods **A 559**, 384 (2006); C.B. Winkelmann, *et al.*, Nucl. Instrum. Methods **A 574**, 264 (2007).
- [33] J.M. Doyle and S.K. Lamoreaux, Europhys. Lett. **26**, 253 (1994); P.R. Huffman, *et al.*, Nature **403**, 62 (2000); D.N. McKinsey, *et al.*, Phys. Rev. **A 67**, 062716 (2003); D.N. McKinsey, *et al.*, Nucl. Instrum. Methods **A 516**, 475 (2004).
- [34] R. Golub and S.K. Lamoreaux, Phys. Rep. **237**, 1 (1994).
- [35] D.H. Beek, *et al.*, arXiv:1111.1273.
- [36] C.F. Barnett and H.K. Reynolds, Phys. Rev. **109**, 355 (1958).
- [37] P. Rudnick, Phys. Rev. **38**, 1342 (1931).
- [38] P. Hvelplund and E. Horsdal Pedersen, Phys. Rev. **A 9**, 2434 (1974).
- [39] W.H. Cramer and J.H. Simons, J. Chem. Phys., **26**, 1272 (1957).
- [40] R. Hegerberg, T. Stefansson, and M.T. Elford, J. Phys. **B 11**, 133 (1978).
- [41] R.D. DuBois, Phys. Rev. **A 39**, 4440 (1989).
- [42] L.I. Pivovarov, V.M. Tubaev, and M.T. Novikov, Sov. Phys. JETP **14**, 20 (1962).
- [43] M.E. Rudd, T.V. Goffe, A. Itoh, and R.D. DuBois, Phys. Rev. **A 32**, 829 (1985).
- [44] R.D. Rivarola and R.D. Picentini, Phys. Rev. **A 20**, 1816 (1979).
- [45] T.P. Grozdanov and R.K. Janev, J. Phys. **B 13**, 3431 (1980).
- [46] M.J. Fulton and M.H. Mittleman, Proc. Phys. Soc., London, **87**, 669 (1966).
- [47] L.I. Pivovarov, M.T. Novikov, and V.M. Tubaev, Sov. Phys. JETP **15**, 1035 (1962).
- [48] G.R. Hertel and W.S. Koski, J. Chem. Phys., **40**, 3452 (1964).
- [49] W. Stich, H.J. Luedde, and R.M. Dreizler, J. Phys. **B 18**, 1195 (1985).
- [50] S.K. Allison, Rev. Mod. Phys., **30**, 1137 (1958).
- [51] W.K. Wu, B.A. Huber, and K. Wiesemann, At. Data. Nucl. Data Tables, **40**, 57 (1988); P. Hvelplund, J. Heinemier, E.H. Pedersen, and F.R. Simpson, J. Phys. **B 9**, 491 (1976).
- [52] M.J. Berger, J.S. Coursey, M.A. Zucker, and J. Chang, "Stopping-Power and Range Tables for Electrons, Protons, and Helium Ions", NIST Standard Reference database Number 124, Oct 1998, National Institute of Standards and Technology, Gaithersburg MD (<http://webbook.nist.gov>).
- [53] S. Sato, K. Kowari, and K. Okazaki, Bull. Chem. Soc. Jap., **49**, 933 (1976).
- [54] L.H. Thomas, Proc. Camb. Phil. Soc., **23**, 829 (1927).
- [55] J. Lindhard and M. Scharff, Phys. Rev. **124**, 128 (1961).
- [56] H.C. Hayden and N.G. Utterback, Phys. Rev. **135**, A1575 (1964).
- [57] C.F. Barnett and P.M. Stier, Phys. Rev. **109**, 385 (1958).
- [58] L.J. Puckett, G.O. Taylor, and D.W. Martin, Phys. Rev. **178**, 271 (1969).
- [59] R.D. DuBois, Phys. Rev. **A 36**, 2585 (1987).
- [60] A.C.F. Santos, W.S. Melo, M.M. Sant'Anna, G.M. Sigaud, and E.C. Montenegro, Phys. Rev. **A 63**, 062717 (2001).
- [61] M.B. Shah and H.B. Gilbody, J. Phys. B: At. Mol. Phys. **18**, 899 (1985).
- [62] V. Kempter, V. Veith, and L. Zehnle, J. Phys. B: Atom. Molec. Phys., **8**, 1041 (1975).
- [63] F.J. De Heer and J. Van Den Bos, Physica, **31**, 365 (1965).
- [64] L.H. Toburen, W.E. Wilson, and R.J. Popowich, Radiat. Res., **82**, 27 (1980).
- [65] S. Uehara and H. Nikjoo, J. Phys. Chem. **B 106**, 11051 (2002).
- [66] S. Sato, K. Kowari, and S. Ohno, Bull. Chem. Soc. Jap., **47**, 2174 (1974).
- [67] J.A. Hornbeck and J.P. Molnar, Phys. Rev. **84**, 621 (1951).
- [68] J. Berkowitz, J. Phys. **B 30**, 881 (1997).
- [69] M. Ovchinnikov, B.L. Grigorenko, K.C. Janda, and V.A. Apkarian, J. Chem. Phys. **108**, 93511 (1998).
- [70] J.P. Hernandez and M.J. Silver, Phys. Rev. **A 2**, 1949 (1970).
- [71] W. Guo, D. Jin, G.M. Seidel and H.J. Maris, Phys. Rev. **B 79**, 054515 (2009).
- [72] W. Guo, M. Dufault, S.B. Cahn, J.A. Nikkel, Y. Shin, and D.N. McKinsey, JINST **7**, P01002 (2012).
- [73] T.M. Ito, S.M. Clayton, J. Ramsey, M. Karcz, C.Y. Liu, J.C. Long, H.O. Meyer, T.G. Reddy, and G.M. Seidel, Phys. Rev. **A 85**, 042718 (2012).
- [74] J.S. Adams, Ph.D. thesis, Brown University, 2001.
- [75] W.P. Jesse and J. Sadauskis, Phys. Rev. **97**, 1668 (1955).
- [76] N. Ishida, J. Kikuchi, and T. Doke, Jpn. J. Appl. Phys. **31**, 1465 (1992) and references therein.

- [77] L. Onsager, Phys. Rev. **54**, 554 (1938).
- [78] G. Jaffe, Ann. Phys. **42**, 303 (1913).
- [79] H.A. Kramers, Physica **18**, 665 (1952).
- [80] A. Ghosh, Ph.D. Thesis (Chapter 8), Brown University, (2005).
- [81] B. Sethumadhavan, Ph.D. thesis (Chapter 7), Brown University, 2007.
- [82] D.N. McKinsey, Ph.D. thesis, Harvard University, 2002.
- [83] D.N. McKinsey *et al.*, Phys. Rev. **A 59**, 200 (1999).
- [84] J.W. Keto, F.J. Soley, M. Stockton, and W.A. Fitzsimmons, Phys. Rev. **A 10**, 872-886 (1974).
- [85] R. Mehrotra, *et al.*, J. Low Temp. Phys. **36**, 47 (1979).
- [86] D.E. Zmeev, F. Pakpour, P.M. Walmsley, A.I. Golov, W. Guo, D.N. McKinsey, G.G. Ihas, W.F. Vinen, and P.V.E. McClintock, J. Low Temp. Phys., DOI10.1007/s10909-012-0720-6, (2012).
- [87] H.A. Roberts and F.L. Hereford, Phys. Rev. **A 7**, 284 (1973).
- [88] D. N. McKinsey *et al.*, Phys. Rev. Lett. **95**, 111101 (2005).
- [89] G. Plante *et al.*, Phys. Rev. **C 84**, 045805 (2011).
- [90] A. Manzur, A. Curioni, L. Kastens, D.N. McKinsey, K. Ni, and T. Wongjirad, Phys. Rev. **C 81**, 025808 (2010).
- [91] A. Manalaysay, PhD thesis, University of Florida, 2010.
- [92] J.C. Long, *et al.*, arXiv:physics/0603231.
- [93] T.M. Ito, J. Phys. Conf. Ser. **69**, 012037 (2007).
- [94] D.H. Beck, D. Budker, B.K. Park, (nEDM Collaboration), arXiv:1111.1273.
- [95] E. Aprile, K.L. Giboni, P. Majewski, K. Ni, and M. Yamashita, IEEE Trans. Nucl. Sci. **51**, 1986-1990 (2004).
- [96] P. Benetti, *et al.*, Astropart. Phys. **28**, 495-507 (2008).
- [97] A.I. Bolozdynya, *Emission Detectors* (World Scientific Publishing Company, 1 edition, 2010).
- [98] C.A.N. Conde and A.J.P.L. Policarpo, Nucl. Instr. Meth. **53**, 7-12 (1967).
- [99] A. Buzulutskov, J. Dodd, R. Galea, Y. Ju, M. Leltchouk, P. Rehak, V. Tcherniatine, W. J. Willis, A. Bondar, D. Pavlyuchenko, R. Snopkov, and Y. Tikhonov, Nucl. Instr. Meth. Phys. Res. **A 548**, 487-498 (2005).
- [100] A.F. Buzulutskov, J. Instrum., **7**, C02025 (2012).
- [101] A. Breskin, R. Alon, M. Cortesi, R. Chechik, J. Miyamoto, V. Dangendorf, J. Maia, J.M.F. Dos Santos, Nucl. Instrum. Meth. **A 598**, 107-111 (2009).
- [102] D. Akimov, *et al.*, arXiv:1204.6218.
- [103] F. Paschen, Annalen der Physik, **273**, 69-96 (1889).
- [104] J. Gerhold, Cryogenics, **12**, 340-416 (1972).
- [105] T. Satow, Cryogenics, **38**, 1145-1153 (1998).
- [106] H. Winkelnkemper, Z. Krasucki, J. Gerhold, and T.W. Dakin, Electra, **52**, 67-86 (1977).
- [107] S.W. Van Sciver, *Helium Cryogenics*, Springer, 2nd ed., 2012.
- [108] R.J. Donnelly and C.F. Barenghi, J. Phys. Chem. Ref. Data **27**, 1217 (1998).
- [109] Y.L. Ju, Y. Gu, J. Dodd, R. Galea, M. Leltchouk, W. Willis, P. Rehak, and V. Tcherniatine, Chin. Sci. Bull. **52**, 3011-3015 (2007).
- [110] Y.L. Ju, *et al.*, Cryogenics, **47**, 81-88 (2007).
- [111] P. Galea, *et al.*, IEEE Trans. Nucl. Sci. **53**, 2260 (2006).
- [112] J. Miyamoto, *et al.*, J. Instrum., **5**, P05008 (2010).
- [113] A. Breskin, V. Peskov, M. Cortesi, R. Budnik, R. Chechik, S. Duval, D. Thers, A.E.C. Coimbra, J.M.F. dos Santos, J.A.M. Lopes, C.D.R. Azevedo, J.F.C.A. Veloso, Nucl. Instrum. Meth. **A 639**, 117-120 (2011).
- [114] P.K. Lightfoot, G.J. Barker, K. Mavrokoridis, Y.A. Ramachers and N.J.C. Spooner, J. Instrum., **4**, P04002 (2009).
- [115] A. Alessandrello, *et al.*, Phys. Rev. Lett. **82**, 513 (1999).
- [116] K.D. Irwin, *et al.*, Nucl. Instrum. Meth. **A 444**, 184 (2000).
- [117] B. Cabrera, J. Low Temp. Phys. **151**, 82 (2008).
- [118] S.R. Bandler, C. Enss, R.E. Lanou, H.J. Maris, T. More, F.S. Porter, and G.M. Seidel, J. Low Temp. Phys., **93**, 709-714 (1993).
- [119] Y.H. Kim, *et al.*, Nucl. Inst. Meth. Phys. Res. **A 520**, 208-211 (2004).
- [120] Y.H. Kim, PhD. thesis, Brown University, 2004.
- [121] N.E. Booth, B. Cabrera, E. Fiorini, Ann. Rev. Nucl. Sci. **46**, 471 (1996).
- [122] K. Pretzl, Nucl. Inst. Meth. **A 454**, 114 (2000).
- [123] R.J. Donnelly, *Quantized Vortices in Helium II*, Cambridge University Press, Cambridge, UK, 2005.
- [124] L. Bruschi, B. Maraviglia, and P. Mazzoldi, Phys. Rev. **143**, 84-90 (1966).
- [125] A. Phillips and P.V.E. McClintock, Phys. Rev. Lett. **33**, 1468 (1974).
- [126] D.R. Allum, R.M. Bowley, and P.V.E. McClintock, Phys. Rev. Lett. **36**, 1313 (1976).
- [127] G.G. Nancolas, T. Ellis, P.V.E. McIntock, and R.M. Bowley, Nature **316**, 197 (1985).
- [128] R.M. Bowley and F.W. Sheard, Phys. Rev. **B 16**, 244 (1977).
- [129] M.A.H. Tucker and A.F.G. Wyatt, Science, **1150**, 283 (1999).
- [130] I.V. Tanatarov, I.N. Adamenko, K.E. Nemchenko, A.F.G. Wyatt, J. Low Temp. Phys. **159**, 549-575 (2010).
- [131] D.N. McKinsey and J.M. Doyle, J. Low Temp. Phys. **118**, 153-165 (2000).
- [132] M.K. Harrison, W.H. Lippincott, D.N. McKinsey, and J.A. Nikkel, Nucl. Instrum. Meth. **A 570**, 556 (2006).
- [133] D.C. Malling, *et al.*, arXiv:1110.0103.
- [134] Y.H. Huang, R.E. Lanou, H.J. Maris, G.M. Seidel, B. Sethumadhavan, and W. Yao, Astropart. Phys. **30**, 1-11 (2008).
- [135] [DAMIC] J. Barreto, *et al.*, Phys. Lett. **B 711**, 264 (2012).
- [136] [DAMA] DAMA/LIBRA first results, European Physics Journal **C56**, 333 (2008), arXiv:0804.2741, as interpreted in Savage *et al.*, arXiv:0808.3607v2.